Available online at www.sciencedirect.com
ScienceDirect
Comput. Methods Appl. Mech. Engrg. 400 (2022) 115511
Computer methods in applied mechanics and engineering
www.elsevier.com/locate/cma

Updated Lagrangian unsaturated periporomechanics for extreme large deformation in unsaturated porous media

Shashank Menon, Xiaoyu Song*

Department of Civil and Coastal Engineering, University of Florida, Gainesville, FL 32611, United States of America

Received 7 February 2022; received in revised form 27 June 2022; accepted 2 August 2022
Available online 28 August 2022

Abstract

Unsaturated periporomechanics is a strong nonlocal poromechanics based on peridynamic state and effective force state concept. In the previous periporomechnics the total Lagrangian formulation is adopted for the solid skeleton of porous media. In this article as a new contribution we formulate and implement an updated Lagrangian unsaturated periporomechanics framework for modeling extreme large deformation in unsaturated soils under drained conditions. In this new framework the so-called bond-associated sub-horizon concept is utilized to enhance the stability and accuracy at extreme large deformation of the solid skeleton. The stabilized nonlocal velocity gradient in the deformed configuration is used to update the effective force state from a critical state based visco-plastic constitutive model for unsaturated soils. The updated Lagrangian periporomechanics paradigm is numerically implemented through an explicit Newmark scheme for high-performance computing. Numerical examples are presented to demonstrate the stability of the computational updated Lagrangian periporomechanics paradigm and its efficacy and robustness in modeling extreme large deformation in porous media under drained conditions.

Keywords: Periporomechanics; Unsaturated porous media; Peridynamics; Extreme large deformation; Stabilization; Updated Lagrangian

1. Introduction

Unsaturated periporomechanics (e.g., [1–5]) is a strong nonlocal formulation of classical poromechanics (e.g., [6–12]) based on peridynamic state [13,14] and effective force state concept [3]. In periporomechanics the solid skeleton of porous media is described by the total Lagrangian framework [1,15,16], following the lines in the original peridynamics for solids (e.g., [13,14,17,18]). Thus, the periporomechanics inherits the significant advantage of the original peridynamics for solids in dealing with discontinuities, long range force, and nonlocality (including less numerical grid dependency). Meanwhile, because the governing equations of periporomechanics are formulated based on integral equations in space, the periporomechanics paradigm is a legitimate computational tool for modeling extreme large deformation in unsaturated porous media, which is the focus of the present contribution. We refer to [4] for detailed discussions on the periporomechanics and local continuum-based numerical methods for modeling unsaturated porous media. The total Lagrangian framework for porous solids could become unreliable if extreme large deformation occurs (e.g., [7,19–21], among others). In peridynamics for single-phase solids, a

* Corresponding author.
E-mail address: xysong@ufl.edu (X. Song).

https://doi.org/10.1016/j.cma.2022.115511
0045-7825/

few studies have been focused on updated Lagrangian or Eulerian formulations (e.g., [22–24]). Bergel and Li [22] proposed an updated Lagrangian peridynamic model for solids in which the horizon of a material point is updated in the deformed configuration. The influence function [14] is determined in terms of the relative position of material points in the deformed configuration. The deformation gradient operator and shape tensor are reformulated in the updated Lagrangian framework. Silling et al. [24] presented a Eulerian peridynamic model that defines bond forces based on only the current configuration. In [24] the authors demonstrated the thermodynamic consistency of the formulation and the efficacy of the formulation in modeling shock waves and fluid motion. While the Eulerian peridynamic formulation in [24] is robust in the aforementioned applications, it is difficult to simulate path-dependent deformation, e.g., plasticity or viscoplasticity. In this article we formulate an updated Lagrangian unsaturated periporomechanics paradigm for simulating extreme large deformation in unsaturated porous media under drained conditions (i.e., constant matric suction) [8]. In this updated Lagrangian periporomechanics paradigm, it is hypothesized that the horizon of a mixed material point is the same uniform sphere as in the reference and current/deformed configurations of the solid skeleton. In line with this hypothesis, the internal variables of the plastic or viscoplastic constitutive model are stored on Lagrangian material points. In this new framework, the multiphase correspondence constitutive principle in periporomechanics [3,4] is reformulated in the updated Lagrangian framework, which will be discussed in what follows.

It is known that both the original single-phase (i.e., solids) and multiphase (i.e., porous media) peridynamic correspondence constitutive models exhibit zero-energy deformation mode instability (e.g., [5,14,16,25]). Silling [25] showed that the numerical oscillation in peridynamic correspondence constitutive models for solids is a material instability instead of a pure numerical instability related to the spatial meshless discretization [26]. The reasons of instability and numerical oscillations are (i) the weak dependence of the force state in a bond on its own deformation and (ii) the loss of the non-uniform deformation due to the integration over the whole horizon of a material point. In [5] the authors demonstrated that the multiphase correspondence principle in periporomechanics inherits the zero-energy mode instability in the original peridynamic correspondence principle [14]. We note that numerous techniques have been proposed to circumvent the instability of the original peridynamic correspondence constitutive model for solids under extreme large deformation and/or dynamic loading (e.g., [25,27–31,31–34], among others). One technique that could eliminate the instability of peridynamic correspondence material models is the so-called sub-horizon or bond-associated peridynamic correspondence material model [31,32,35]. In [35], the authors proposed to decompose the spherically symmetric horizon into discrete sub-horizons that would effectively disturb the radial symmetry of peridynamics. At a material point, each sub-horizon has its own deformation gradient that can remove the smoothing effect of assembling the deformation gradient over the entire horizon. Chen [32] formulated a bond-associated peridynamics for correspondence material models for solids which is consistent with the sub-horizon concept. Different from the work in [35] the sub-horizons are associated with individual bonds and include only the neighboring material points that are around the bond (i.e., sub-horizon). Gu et al. [31] enhanced the bond-associated sub-horizon peridynamics using the higher-order deformation gradient to improve its accuracy for modeling solids. Note the sub-horizon or bond-associated peridynamics was proposed for stabilizing peridynamic correspondence constitutive models for single-phase solids. Recently the authors [5] formulated a stabilized multiphase correspondence principle for unsaturated periporomechanics in the total Lagrangian framework.

In this study, as a new contribution, we demonstrate that the updated Lagrangian periporomechanics formulation inherits the stability issue of the original multiphase correspondence principle in the total Lagrangian formulation of solid skeleton in periporomechanics. Then we implement the bond-associated sub-horizon concept to stabilize the formulated updated Lagrangian periporomechanics. The updated Lagrangian periporomechanics paradigm is numerically implemented through an explicit Newmark scheme with Open MPI [36] for high-performance computing. Numerical examples are presented to demonstrate the efficacy of the updated Lagrangian periporomechanics and its robustness in modeling unsaturated soil column collapse under drained conditions. We model unsaturated soil column collapse with the proposed stabilized updated Lagrangian periporomechanics framework in that the soil column collapse is of great relevance in a number of geological and industrial processes such as debris flows [37,38], landslides [39,40] and pyroclastic flows [41,42]. For instance, debris flows during avalanches and mudslides are major geohazards on Earth because debris can travel extensive distances and destroy civil infrastructure such as buildings and roadways. For this reason, numerous studies of this subject through physical testing and numerical modeling have been reported (e.g., [43–48]). We refer to the literature ([7,40,46,48–52], among others) for computational methods based on classical local continuum theory for modeling large deformation in unsaturated porous media.

We note that due to its natural nonlocality the updated Lagrangian peridynamics paradigm is computationally more demanding than other continuum-based computational methods (e.g., the finite element method) for modeling the mechanics and physics of porous media. Therefore, in this study parallel computing through Open MPI is utilized for computational efficiency. We refer to the literature for coupling peridynamics with the finite element method for modeling solid deformation and fluid flow respectively in porous materials (e.g., [53,54]). As a brief summary, the original contributions of this article include (i) the formulation of an updated Lagrangian peridynamics model for extreme large deformation in unsaturated porous media under drained conditions (i.e., one-way coupling), (ii) the proof of the lack of stability of the original total Lagrangian multiphase constitutive correspondence principle in the updated Lagrangian framework and the stabilization through the bond-associated sub-horizon concept, (iii) the numerical implementation for high-performance computing through an explicit Newmark scheme, and (iv) the demonstration of efficacy of the newly implemented numerical paradigm in modeling extreme large deformation in porous media under drained conditions. For sign convention, the assumption in continuum mechanics is followed, i.e., for the solid skeleton, tensile force/stress is positive and compression is negative, and for fluid pressure compression is positive and tension is negative.

2. Updated Lagrangian unsaturated peridynamics

Peridynamics has been formulated based on the total Lagrangian approach [3,4] in which the deformation of solid skeleton is referred to the reference/undeformed configuration of skeleton and the fluid flow is described through the relative Eulerian framework referring to the skeleton in the current configuration. In peridynamics, it is hypothesized that a porous media body can be conceptualized as a collection of a finite number of mixed material points with two kinds of degree of freedom, i.e., displacement and fluid pressure. A material point $\boldsymbol{X}$ has poromechanical and physical interactions with any material point $\boldsymbol{X}'$ within its neighborhood, $\mathcal{H}$. Here $\mathcal{H}$ is a spherical domain around $\boldsymbol{X}$ with radius δ, i.e., the horizon for the porous medium, the initial configuration. A stabilized multiphase constitutive correspondence principle (e.g., [3,5]) has been proposed to incorporate the classical constitutive models for unsaturated soils and physical laws for unsaturated fluid flow in porous media. In this section we reformulate the total Lagrangian peridynamics paradigm using the updated Lagrangian framework for modeling extreme large deformation in unsaturated porous media under drained conditions (i.e., constant matric suction).

2.1. Updated Lagrangian formulation

For the updated Lagrangian peridynamics, the equation of motion of a porous body is formulated referring to the current (i.e., deformed) configuration instead of the initial (i.e., undeformed) configuration of the same porous body. Fig. 1 schematically represents 3 configurations of a porous material body, i.e., the initial/undeformed configuration, current configuration and next configuration following the current configuration. For conciseness of notations, in the current configuration the peridynamic state variable without a prime denotes the variable evaluated at $\boldsymbol{x}$ on the associated bond $\boldsymbol{x}'-\boldsymbol{x}$ and the peridynamic state variable with a prime stands for the variable evaluated at $\boldsymbol{x}'$ on the associated bond $\boldsymbol{x}-\boldsymbol{x}'$, e.g., $\underline{\mathscr{T}} = \underline{\mathscr{T}}[\boldsymbol{x}]\langle \boldsymbol{x}'-\boldsymbol{x}\rangle$ and $\underline{\mathscr{T}}' = \underline{\mathscr{T}}[\boldsymbol{x}']\langle \boldsymbol{x}-\boldsymbol{x}'\rangle$.

The spatial positions of materials points $\boldsymbol{X}$ and $\boldsymbol{X}'$ in the initial/undeformed configuration are denoted by $\boldsymbol{x}$ and $\boldsymbol{x}'$ in the current/deformed configuration, respectively. Let $\boldsymbol{u}$ and $\boldsymbol{u}'$ be the displacement vectors of $\boldsymbol{x}$ and $\boldsymbol{x}'$ referring to the current configuration. The bond between $\boldsymbol{x}$ and $\boldsymbol{x}'$ is denoted by $\boldsymbol{\zeta}$, i.e., $\boldsymbol{\zeta} = \boldsymbol{x}'-\boldsymbol{x}$. For the updated Lagrangian peridynamics formulation, it is assumed that the horizon δ is constant. In this sense, the family $\mathscr{H}$ (i.e., horizon) of a material point $\boldsymbol{X}$ in the current configuration is defined as

$$\mathscr{H} := \{\boldsymbol{x}' | \boldsymbol{x}' \in \mathscr{B}, 0 \leq |\underline{\boldsymbol{\zeta}}| \leq \delta\}, \tag{1}$$

where $\mathscr{B}$ denotes a porous media body. Note this assumption is consistent with the Eulerian formulation of peridynamics for solids in [24]. However, the material points of solid skeleton are described by their motions. In this sense, with deformation, the set of material points in the horizon of material point $\boldsymbol{x}$ can be different from time to time in extreme large deformation regime. Therefore, with this assumption the extreme distortion of the horizon for extreme large deformation of the solid skeleton in the total Lagrangian formulation can be avoided. As

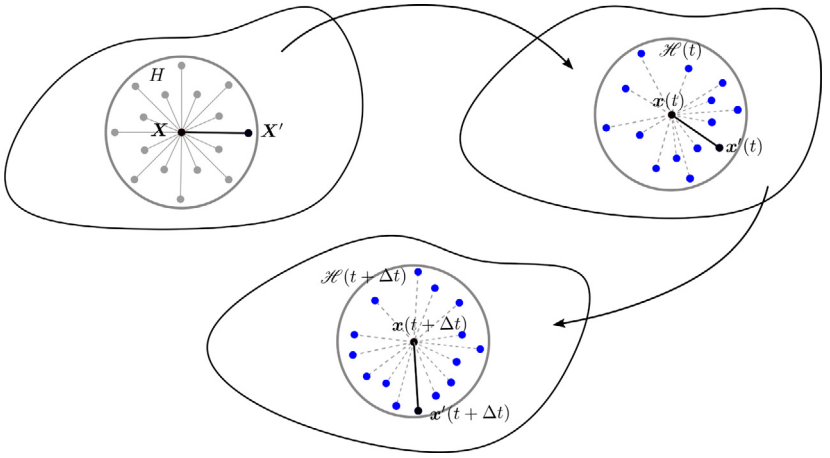

Fig. 1. Schematic depiction of the kinematics of the solid skeleton in the updated Lagrangian formulation: initial configuration, current configuration (reference), and next configuration.

in the total Lagrangian formulation, in the updated Lagrangian formulation the total force vector state at material point $\boldsymbol{x}$ along bond $\boldsymbol{\zeta}$ under the assumption of passive pore air pressure can be decomposed into

$$\underline{\mathscr{T}} = \overline{\underline{\mathscr{T}}} - S_r \underline{\mathscr{T}}_w, \tag{2}$$

where $\overline{\underline{\mathscr{T}}}$ and $\underline{\mathscr{T}}_w$ are the effective force state of the porous media and the water force state, respectively, and S_r is the degree of saturation in the current configuration. Assuming weightless pore air the density ρ of the mixture can be written as

$$\rho = \rho_s(1-\phi) + S_r \rho_w \phi, \tag{3}$$

where ρ_s is the intrinsic density of the solid and ρ_w is the intrinsic density of water, and ϕ is the porosity in the current configuration.

Let $\boldsymbol{u}$ be the displacement vector of material point $\boldsymbol{x}$ in the current configuration. Following the lines in the total Lagrangian peridynamics [2], the equation of motion of the updated Lagrangian peridynamics can be written as

$$\rho \ddot{\boldsymbol{u}} = \int_{\mathscr{H}} (\underline{\mathscr{T}}[\boldsymbol{x}]\langle\underline{\boldsymbol{\zeta}}\rangle - \underline{\mathscr{T}}'[\boldsymbol{x}']\langle\underline{\boldsymbol{\zeta}}'\rangle)\, \mathrm{d}\mathscr{V}' + \rho \boldsymbol{g}, \tag{4}$$

where $\underline{\mathscr{T}}[\boldsymbol{x}]\langle\underline{\boldsymbol{\zeta}}\rangle$ and $\underline{\mathscr{T}}'[\boldsymbol{x}']\langle\underline{\boldsymbol{\zeta}}'\rangle$ are the total force vector states at material points $\boldsymbol{x}$ and $\boldsymbol{x}'$, respectively, in the current configuration, $\ddot{\boldsymbol{u}}$ is the acceleration vector, and $\boldsymbol{g}$ is gravity acceleration vector.

Following [14], the spatial shape tensor $\mathscr{K}$ in the current configuration can be defined as

$$\mathscr{K} = \int_{\mathscr{H}} \underline{\omega}\langle\underline{\boldsymbol{\zeta}}\rangle\, \underline{\boldsymbol{\zeta}} \otimes \underline{\boldsymbol{\zeta}}\, \mathrm{d}\mathscr{V}', \tag{5}$$

where $\underline{\omega}\langle\underline{\boldsymbol{\zeta}}\rangle$ is the influence function. Then it follows from the notion of original reduction operator [14,18] (i.e., referring to the initial configuration), we can define the spatial gradient operator [22] in the current configuration as

$$\mathscr{G}(z) = \left[\int_{\mathscr{H}} \underline{\omega}\langle\underline{\boldsymbol{\zeta}}\rangle (z'-z) \otimes \underline{\boldsymbol{\zeta}}\, \mathrm{d}\mathscr{V}'\right] \mathscr{K}^{-1}, \tag{6}$$

where z' and z are vector variables at material points $\boldsymbol{x}'$ and $\boldsymbol{x}$, respectively. Using (6) we can define the velocity gradient $\mathscr{L}$. Recall from nonlinear continuum mechanics that $\mathscr{L}$ as the spatial gradient of the velocity vector $\dot{\boldsymbol{u}}$ reads

$$\mathscr{L} = \frac{\partial \dot{\boldsymbol{u}}}{\partial \boldsymbol{x}}. \tag{7}$$

Next, it follows from (6) and (7) we obtain the nonlocal velocity gradient as

$$\mathscr{L} = \mathscr{G}(\dot{\boldsymbol{u}}) = \left(\int_{\mathscr{H}} \underline{\omega}\, \underline{\dot{\mathscr{Y}}} \otimes \underline{\boldsymbol{\zeta}}\, \mathrm{d}\mathscr{V}' \right) \mathscr{K}^{-1}, \tag{8}$$

where $\underline{\mathscr{Y}} = \boldsymbol{y}' - \boldsymbol{y}$ is the deformation state in the current configuration, and $\boldsymbol{y} = \boldsymbol{x} + \boldsymbol{u}$. Given (8), the rate of nonlocal deformation can be readily obtained as

$$\mathscr{D} = \frac{1}{2}[\mathscr{L} + \mathscr{L}^T]. \tag{9}$$

The rate of deformation tensor can be used to determine the effective Cauchy stress tensor $\overline{\boldsymbol{\sigma}}$ through a classical elastoplastic constitutive model for unsaturated soils (e.g., [1,55–58]). Then, the rate form of the strain energy of the solid skeleton of an unsaturated porous material body $\mathscr{B}$ under pure elastic deformation reads [3,14]

$$\begin{aligned}
\dot{\mathscr{W}} &= \int_{\mathscr{B}} \overline{\sigma}_{ij} \mathscr{D}_{ij}\, \mathrm{d}\mathscr{V} \\
&= \int_{\mathscr{B}} \overline{\sigma}_{ij} \mathscr{L}_{ij}\, \mathrm{d}\mathscr{V} \\
&= \int_{\mathscr{B}} \overline{\sigma}_{ij} \left(\int_{\mathscr{H}} \underline{\omega \dot{\mathscr{Y}}}_i \underline{\zeta}_p\, \mathrm{d}\mathscr{V}' \right) \mathscr{K}^{-1}_{pj}\, \mathrm{d}\mathscr{V} \\
&= \int_{\mathscr{B}} \left(\int_{\mathscr{H}} \underline{\omega \dot{\mathscr{Y}}}_i \underline{\zeta}_p\, \mathrm{d}\mathscr{V}' \right) \mathscr{K}^{-1}_{pj} \overline{\sigma}_{ji}\, \mathrm{d}\mathscr{V} \\
&= \int_{\mathscr{B}} \int_{\mathscr{B}} \underline{\omega \zeta}_p \mathscr{K}^{-1}_{pj} \overline{\sigma}_{ji} \underline{\dot{\mathscr{Y}}}_i\, \mathrm{d}\mathscr{V}'\, \mathrm{d}\mathscr{V},
\end{aligned} \tag{10}$$

where $i, j, p = 1, 2, 3$. The rate of strain energy of the solid skeleton of porous media under pure elastic deformation referring to the current configuration reads [3]

$$\dot{\mathscr{W}} = \int_{\mathscr{B}} \int_{\mathscr{B}} \underline{\overline{\mathscr{T}}}_i\, \underline{\dot{\mathscr{Y}}}_i\, \mathrm{d}\mathscr{V}' \mathrm{d}\mathscr{V}. \tag{11}$$

It follows from (10) and (11) that the effective force state can be expressed as

$$\underline{\overline{\mathscr{T}}} = \underline{\omega \boldsymbol{\zeta}} \mathscr{K}^{-1} \overline{\boldsymbol{\sigma}}. \tag{12}$$

Through the effective force state concept (see Eq. (2)) the fluid force state can be expressed as

$$\underline{\mathscr{T}}_w = \underline{\omega \boldsymbol{\zeta}} \mathscr{K}^{-1} (p_w \mathbf{1}), \tag{13}$$

where $\mathbf{1}$ is the second-order identity tensor.

Finally, substituting (12), (2) and (13) into (4) the motion of equation can be written as

$$\rho \ddot{\boldsymbol{u}} = \int_{\mathscr{H}} \left[\underline{\omega \boldsymbol{\zeta}} \mathscr{K}^{-1} (\overline{\boldsymbol{\sigma}} - S_r p_w \mathbf{1}) - \underline{\omega}'\, \underline{\boldsymbol{\zeta}}' \mathscr{K}'^{-1} (\overline{\boldsymbol{\sigma}}' - S'_r p'_w \mathbf{1}) \right] \mathrm{d}\mathscr{V}' + \rho \boldsymbol{g}. \tag{14}$$

The degree of saturation S_r can be determined from the soil–water retention curve (e.g., [59–63]) that depends on the volume strain of the solid skeleton (e.g., porosity). In this study, we adopt the one in [19,20,64] which reads

$$S_r(\mathscr{J}, \phi, p_w) = \left\{ 1 + \left[-\alpha_1 \left(\frac{\mathscr{J}}{1-\phi} - 1 \right)^{\alpha_2} \mathscr{J}\, p_w \right]^{\alpha_3} \right\}^{(\alpha_3 - 1)/\alpha_3}, \tag{15}$$

where α_1, α_2, and α_3 are all material parameters. The evolution of porosity can be written as

$$\phi(\mathscr{J}) = 1 - \frac{(1-\phi)}{\mathscr{J}}, \tag{16}$$

where $\mathscr{J}$ is the determinant of the spatial deformation gradient $\mathscr{F}$.

From (6), the spatial deformation gradient can be written as

$$\mathscr{F} = \mathscr{G} = \left[\int_{\mathscr{H}} \underline{\omega}\, \underline{\mathscr{Y}} \otimes \underline{\boldsymbol{\zeta}}\, \mathrm{d}\mathscr{V}' \right] \mathscr{K}^{-1}. \tag{17}$$

It can be proved as follows. Given that the spatial deformation gradient $\boldsymbol{\mathcal{F}}$ maps $\underline{\boldsymbol{\zeta}}$ onto $\underline{\boldsymbol{\mathcal{Y}}}$

$$\underline{\boldsymbol{\mathcal{Y}}} = \boldsymbol{\mathcal{F}}\underline{\boldsymbol{\zeta}}. \tag{18}$$

Substituting (18) into (17) generates

$$\begin{aligned}\boldsymbol{\mathcal{G}}(\boldsymbol{x}) &= \int_{\mathcal{H}} \underline{\omega\boldsymbol{\mathcal{Y}}} \otimes \underline{\boldsymbol{\zeta}}\, \mathrm{d}\mathcal{V}' \left[\int_{\mathcal{H}} \underline{\omega}\, \underline{\boldsymbol{\zeta}} \otimes \underline{\boldsymbol{\zeta}}\, \mathrm{d}\mathcal{V}'\right]^{-1} \\ &= \int_{\mathcal{H}} \underline{\omega}(\boldsymbol{\mathcal{F}}\underline{\boldsymbol{\zeta}}) \otimes \underline{\boldsymbol{\zeta}}\, \mathrm{d}\mathcal{V}' \left[\int_{\mathcal{H}} \underline{\omega}\, \underline{\boldsymbol{\zeta}} \otimes \underline{\boldsymbol{\zeta}}\, \mathrm{d}\mathcal{V}'\right]^{-1} \\ &= \boldsymbol{\mathcal{F}} \int_{\mathcal{H}} \underline{\omega\boldsymbol{\zeta}} \otimes \underline{\boldsymbol{\zeta}}\, \mathrm{d}\mathcal{V}' \left[\int_{\mathcal{H}} \underline{\omega\boldsymbol{\zeta}} \otimes \underline{\boldsymbol{\zeta}}\, \mathrm{d}\mathcal{V}'\right]^{-1} \\ &= \boldsymbol{\mathcal{F}}. \end{aligned} \tag{19}$$

In what follows, we demonstrate that the nonlocal spatial deformation gradient defined in (17) only represents the uniform deformation state. Thus the spatial correspondence principle inherits the zero-energy mode instability issue. The nonuniform part of the solid spatial deformation state reads

$$\underline{\boldsymbol{\mathcal{R}}} = \underline{\boldsymbol{\mathcal{Y}}} - \boldsymbol{\mathcal{F}}\underline{\boldsymbol{\zeta}}. \tag{20}$$

Substituting (20) into the spatial nonlocal deformation gradient (17)

$$\begin{aligned}\boldsymbol{\mathcal{F}}\left(\underline{\boldsymbol{\mathcal{R}}}\right) &= \left(\int_{\mathcal{H}} \underline{\omega\boldsymbol{\mathcal{Y}}} \otimes \underline{\boldsymbol{\zeta}}\, \mathrm{d}\mathcal{V}'\right) \boldsymbol{\mathcal{K}}^{-1} \\ &= \int_{\mathcal{H}} \underline{\omega}\, \underline{\boldsymbol{\mathcal{R}}} \otimes \underline{\boldsymbol{\zeta}}\, \mathrm{d}\mathcal{V}' \left(\int_{\mathcal{H}} \underline{\omega}\, \underline{\boldsymbol{\zeta}} \otimes \underline{\boldsymbol{\zeta}}\, \mathrm{d}\mathcal{V}'\right)^{-1} \\ &= \int_{\mathcal{H}} \underline{\omega}\, (\underline{\boldsymbol{\mathcal{Y}}} - \boldsymbol{\mathcal{F}}\underline{\boldsymbol{\zeta}}) \otimes \underline{\boldsymbol{\zeta}}\, \mathrm{d}\mathcal{V}' \left(\int_{\mathcal{H}} \underline{\omega}\, \underline{\boldsymbol{\zeta}} \otimes \underline{\boldsymbol{\zeta}}\, \mathrm{d}\mathcal{V}'\right)^{-1} \\ &= \left(\int_{\mathcal{H}} \underline{\omega}\, (\underline{\boldsymbol{\mathcal{Y}}} \otimes \underline{\boldsymbol{\zeta}})\, \mathrm{d}\mathcal{V}' - \boldsymbol{\mathcal{F}} \int_{\mathcal{H}} \underline{\omega}\, (\underline{\boldsymbol{\zeta}} \otimes \underline{\boldsymbol{\zeta}})\, \mathrm{d}\mathcal{V}'\right) \left(\int_{\mathcal{H}} \underline{\omega}\, \underline{\boldsymbol{\zeta}} \otimes \underline{\boldsymbol{\zeta}}\, \mathrm{d}\mathcal{V}'\right)^{-1} \\ &= \boldsymbol{\mathcal{F}} - \boldsymbol{\mathcal{F}}\boldsymbol{\mathcal{K}}\boldsymbol{\mathcal{K}}^{-1} = \mathbf{0}. \end{aligned} \tag{21}$$

It follows from (21) that the nonuniform part of the deformation state is missing in the spatial deformation gradient. Next, we present a stabilization scheme for the spatial corresponding model for the solid skeleton based on the bond-associated sub-horizon concept.

2.2. Stabilization through the sub-horizon based concept

In this study, we apply the sub-horizon concept (e.g., [31,32,35]) to circumvent the zero-energy mode instability of correspondence material models for solid skeleton in the updated Lagrangian periporomechanics. We refer to the literature for other stabilization techniques (e.g., [5,25,31]). Fig. 2 plots the bond-associated sub-horizon concept both in the initial/reference and current/deformed configurations of a porous material body. As shown in Fig. 2, in the horizon of material point $\boldsymbol{x}$ each bond is endowed with a sub-horizon composed of material points around the bond that is used to determine the nonlocal deformation gradient, the effective stress and the effective force state on that bond. Therefore, the sub-horizon stabilized scheme can guarantee a unique mapping between the deformation state and the force state on each individual bond. We note that the original bond-associated sub-horizon formulation was based on the total Lagrangian approach (i.e., the sub-horizon refers to the initial/undeformed configuration). In the updated Lagrangian periporomechanics formulation, this bond-associated sub-horizon concept is reformulated in the current/deformed configuration with updated material points in the horizon of a material point and the sub-horizon for an individual bond.

Referring to Fig. 2 the sub-horizon $\mathcal{H}_s$ for the bond $\boldsymbol{\zeta}$ at material point $\boldsymbol{x}$ in the current configuration of the solid skeleton reads

$$\mathcal{H}_s = \mathcal{H} \cap \mathcal{H}'. \tag{22}$$

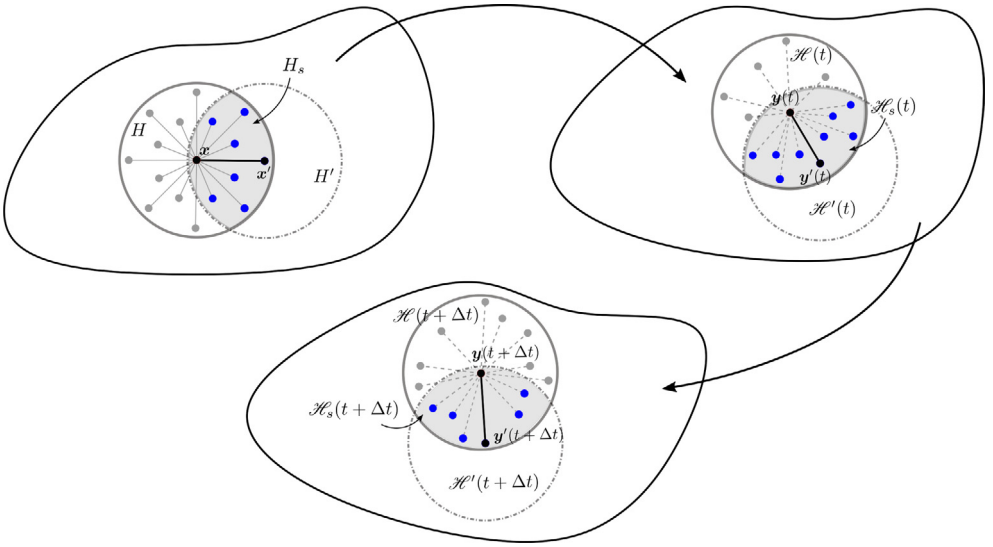

Fig. 2. Schematic of the sub-horizon concept for the updated Lagrangian framework.

It follows from (17), (5) and (22) that the sub-horizon based spatial shape tensor and deformation gradient can be written as

$$\boldsymbol{\mathcal{K}}_s = \int_{\mathscr{H}_s} \omega \, \underline{\boldsymbol{\zeta}} \otimes \underline{\boldsymbol{\zeta}} \, \mathrm{d}\mathscr{V}', \tag{23}$$

$$\boldsymbol{\mathcal{F}}_s = \left(\int_{\mathscr{H}_s} \omega \, \underline{\boldsymbol{\mathcal{Y}}} \otimes \underline{\boldsymbol{\zeta}} \, \mathrm{d}\mathscr{V}' \right) \boldsymbol{\mathcal{K}}_s^{-1}. \tag{24}$$

From (8), the sub-horizon based spatial velocity gradient reads

$$\boldsymbol{\mathcal{L}}_s = \left(\int_{\mathscr{H}_s} \omega \, \underline{\dot{\boldsymbol{\mathcal{Y}}}} \otimes \underline{\boldsymbol{\zeta}} \, \mathrm{d}\mathscr{V}' \right) (\boldsymbol{\mathcal{K}}_s)^{-1}, \tag{25}$$

With (25) the sub-horizon based rate of deformation in the current configuration can be expressed as

$$\boldsymbol{\mathcal{D}}_s = \frac{1}{2}[\boldsymbol{\mathcal{L}}_s + \boldsymbol{\mathcal{L}}_s^T]. \tag{26}$$

Given (26) the effective Cauchy stress tensor $\overline{\boldsymbol{\sigma}}_s$ can be determined in the current configuration through a classical constitutive model.

Next, we derive the effective force state on a bond $\boldsymbol{\zeta}$ at material point $\boldsymbol{x}$ following the lines in the updated Lagrangian formulation in Section 2.1. The rate of strain energy density at $\boldsymbol{x}$ on the bond $\boldsymbol{\zeta}$ that is determined by the bond-associated sub-horizon method can be written as

$$\dot{\overline{\mathscr{W}}}_s\langle\boldsymbol{\zeta}\rangle = \int_{\mathscr{H}_s} \underline{\overline{\boldsymbol{\mathcal{T}}}}_s \cdot \underline{\dot{\boldsymbol{\mathcal{Y}}}} \, \mathrm{d}\mathscr{V}', \tag{27}$$

where $\underline{\overline{\boldsymbol{\mathcal{T}}}}_s$ is the sub-horizon effective force state on the bond $\boldsymbol{\zeta}$ in the current configuration. $\dot{\mathscr{W}}_s\langle\boldsymbol{\zeta}\rangle$ can be related to the rate of total strain energy density $\dot{\overline{\mathscr{W}}}$ at $\boldsymbol{x}$ through a volume fraction factor φ_s as

$$\dot{\overline{\mathscr{W}}}_s\langle\boldsymbol{\zeta}\rangle = \varphi_s \dot{\overline{\mathscr{W}}}, \tag{28}$$

with

$$\varphi_s = \frac{\int_{\mathscr{H}_s} 1 \, \mathrm{d}\mathscr{V}'}{\int_{\mathscr{H}} 1 \, \mathrm{d}\mathscr{V}'}. \tag{29}$$

Given the rate of deformation tensor $\mathscr{D}_s$ the effective Cauchy stress tensor $\overline{\boldsymbol{\sigma}}_s$ can be determined from a local constitutive model. From local theory, the rate of strain energy density at material point $\boldsymbol{x}$ reads

$$\begin{aligned}\dot{\overline{\mathscr{W}}} &= \overline{\boldsymbol{\sigma}}_s : \mathscr{D}_s \\ &= \overline{\boldsymbol{\sigma}}_s : \left(\int_{\mathscr{H}_s} \underline{\omega}\, \underline{\dot{\boldsymbol{y}}} \otimes \underline{\boldsymbol{\zeta}}\, \mathrm{d}\mathscr{V}'\right)(\mathscr{K}_s)^{-1} \\ &= \int_{\mathscr{H}_s} \underline{\omega}\, \underline{\boldsymbol{\zeta}}(\mathscr{K}_s)^{-1}\overline{\boldsymbol{\sigma}}_s \underline{\dot{\boldsymbol{y}}}\, \mathrm{d}\mathscr{V}'. \end{aligned} \tag{30}$$

It follows from (27), (28) and (30) the sub-horizon based effective force state can be expressed as

$$\underline{\overline{\mathscr{T}}}_s = \varphi_s \underline{\omega}\, \underline{\boldsymbol{\zeta}}(\mathscr{K}_s)^{-1}\overline{\boldsymbol{\sigma}}_s. \tag{31}$$

From the effective force state concept and (31), the sub-horizon based total force state reads

$$\underline{\mathscr{T}}_s = \varphi_s \underline{\omega}\, \underline{\boldsymbol{\zeta}}(\mathscr{K}_s)^{-1}(\overline{\boldsymbol{\sigma}}_s - S_r p_w \mathbf{1}). \tag{32}$$

Then, the equation of motion (14) can be rewritten as

$$\rho\ddot{\boldsymbol{u}} = \int_{\mathscr{H}} \left[\varphi_s \underline{\omega}\, \underline{\boldsymbol{\zeta}}(\mathscr{K}_s)^{-1}(\overline{\boldsymbol{\sigma}}_s - S_r p_w \mathbf{1}) - \varphi'_s \underline{\omega}'\, \underline{\boldsymbol{\zeta}}'(\mathscr{K}'_s)^{-1}(\overline{\boldsymbol{\sigma}}'_s - S'_r p'_w \mathbf{1})\right] \mathrm{d}\mathscr{V}' + \rho \boldsymbol{g}. \tag{33}$$

In what follows, we demonstrate that the updated Lagrangian sub-horizon correspondence constitutive model satisfies the sufficient condition (e.g.,[5,25]) that mitigates the zero-energy mode instability. This criterion in terms of the rate form of the effective force state and deformation state can be written as

$$\int_{\mathscr{H}} \underline{\dot{\overline{\mathscr{T}}}} \cdot \underline{\dot{\boldsymbol{y}}} \mathrm{d}\mathscr{V}' > 0. \tag{34}$$

It follows from (31) that this condition can be expressed using the sub-horizon based effective force state as

$$\int_{\mathscr{H}} \left(\int_{\mathscr{H}_s} \underline{\dot{\overline{\mathscr{T}}}} \cdot \underline{\dot{\boldsymbol{y}}} \mathrm{d}\mathscr{V}'\right) \mathrm{d}\mathscr{V}' > 0, \tag{35}$$

where

$$\begin{aligned}\underline{\dot{\overline{\mathscr{T}}}}_i &= \frac{1}{\varphi_s}\underline{\dot{\overline{\mathscr{T}}}}_{s,i} \\ &= \underline{\omega}\, \underline{\zeta}_k \mathscr{K}^{-1}_{s,kj}\dot{\overline{\sigma}}_{s,ji}. \end{aligned} \tag{36}$$

Assuming a local elastic material model, we have

$$\begin{aligned}\dot{\overline{\sigma}}_{s,ij} &= \mathscr{C}_{ijmn}\mathscr{D}_{s,mn} \\ &= \mathscr{C}_{ijmn}\mathscr{L}_{s,mn}, \end{aligned} \tag{37}$$

where $\mathscr{C}_{ijmn}$ is the fourth-order elastic stiffness tensor, and $m, n = 1, 2, 3$. Substituting (37) into (35) yields

$$\begin{aligned}\int_{\mathscr{H}} \left(\int_{\mathscr{H}_s} \underline{\dot{\overline{\mathscr{T}}}} \cdot \underline{\dot{\boldsymbol{y}}} \mathrm{d}\mathscr{V}'\right) \mathrm{d}\mathscr{V}' &= \int_{\mathscr{H}} \left(\int_{\mathscr{H}_s} \left(\underline{\omega}\, \underline{\zeta}_k \mathscr{K}^{-1}_{s,kj} \mathrm{d}\dot{\overline{\sigma}}_{s,ji}\right) \dot{\mathscr{Y}}_i\, \mathrm{d}\mathscr{V}'\right) \mathrm{d}\mathscr{V}' \\ &= \int_{\mathscr{H}} \left(\int_{\mathscr{H}_s} \underline{\omega}\, \underline{\zeta}_k \mathscr{K}^{-1}_{s,kj}\dot{\overline{\sigma}}_{s,ji}\dot{\mathscr{Y}}_i\, \mathrm{d}\mathscr{V}'\right) \mathrm{d}\mathscr{V}' \\ &= \int_{\mathscr{H}} \left(\dot{\overline{\sigma}}_{s,ij} \left(\int_{\mathscr{H}_s} \underline{\omega}\, \dot{\mathscr{Y}}_i\, \underline{\zeta}_k\, \mathrm{d}\mathscr{V}'\right) \mathscr{K}^{-1}_{s,kj}\right) \mathrm{d}\mathscr{V}' \\ &= \int_{\mathscr{H}} \left(\dot{\overline{\sigma}}_{s,ij}\mathscr{L}_{s,ij}\right) \mathrm{d}\mathscr{V}' \\ &= \int_{\mathscr{H}} \left(\mathscr{L}_{s,ij}\mathscr{C}_{ijmn}\mathscr{L}_{s,mn}\right) \mathrm{d}\mathscr{V}' > 0. \end{aligned} \tag{38}$$

It follows from (25) and (38) that (35) holds given $\dot{\boldsymbol{\mathscr{Y}}} > 0$ (i.e., nonzero increment of deformation state). Therefore, the sub-horizon based correspondence constitutive model is stable in the updated Lagrangian formulation. In this

study we assume $\delta = \delta'$ that implies $\mathscr{L}_s = \mathscr{L}'_s$. By this assumption, it will guarantee

$$\underline{\overline{\mathscr{T}}}_s = -\underline{\overline{\mathscr{T}}}'_s. \tag{39}$$

Next, we introduce a classical viscoplastic model for unsaturated porous media that will be implemented in the updated Lagrangian peridynamic framework.

2.3. Constitutive model for unsaturated soil

In this section, we briefly introduce the key elements of a critical state based viscoplasticity model for unsaturated soil using the Perzyna model of viscoplasticity (e.g., [65,66]). For the local viscoplastic constitutive model, the yield function reads

$$f(\overline{p}, q, \overline{p}_c) = \frac{q^2}{M^2} + \overline{p}(\overline{p} - \overline{p}_c), \tag{40}$$

where $\overline{p} = \mathrm{tr}(\overline{\boldsymbol{\sigma}})/3$ is the mean effective stress, $q = \sqrt{3/2}|\overline{\boldsymbol{\sigma}} - \overline{p}\mathbf{1}|$ is the equivalent shear stress, $\overline{\boldsymbol{\sigma}}$ is the effective stress tensor, M is the slope of the critical state line, and $\overline{p}_c$ is the effective pre-consolidation pressure that evolves with the viscoplastic volumetric strain ε_v^{vp} and matric suction (i.e., $-p_w$ assuming passive pore air pressure). The effective mean stress $\overline{p}$ and the shear stress q can be written as

$$\overline{p} = K\varepsilon_v^e, \quad q = 3\mu_s\varepsilon_s^e, \tag{41}$$

where K and μ_s are the elastic bulk and shear moduli, respectively, and $\varepsilon_v^e = \mathrm{tr}(\boldsymbol{\varepsilon}^e)$ and $\varepsilon_s^e = \sqrt{\frac{2}{3}}|\boldsymbol{\epsilon}^e - \frac{1}{3}\varepsilon_v^e\mathbf{1}|$ are elastic volumetric strain and shear strain, respectively.

The total strain rate is decomposed into

$$\dot{\boldsymbol{\varepsilon}} = \dot{\boldsymbol{\varepsilon}}^e + \dot{\boldsymbol{\varepsilon}}^{vp}. \tag{42}$$

Assuming the Perzyna type of viscoplasticity, the rate of viscoplastic strain tensor $\dot{\boldsymbol{\varepsilon}}^{vp}$ can be expressed as

$$\dot{\boldsymbol{\varepsilon}}^{vp} = \frac{\langle f \rangle}{\eta}\frac{\partial f}{\partial \overline{\boldsymbol{\sigma}}}, \tag{43}$$

where η is the viscosity coefficient and $\langle\ \rangle$ is the Macaulay bracket operator

$$\langle f \rangle = \begin{cases} 0 & f \le 0, \\ f & f > 0. \end{cases} \tag{44}$$

The effective apparent pre-consolidation pressure $\overline{p}_c$ [1,67,68] can be written as

$$\overline{p}_c = -\exp(b_1)(-p_c)^{b_2}, \tag{45}$$

where b_1 and b_2 are variables depending on the degree of saturation and matric suction (see [1,67] for more details) and the rate of p_c reads

$$\dot{p}_c = \frac{-p_c}{\tilde{\lambda} - \tilde{\kappa}}\mathrm{tr}(\dot{\boldsymbol{\epsilon}}^{vp}), \tag{46}$$

where $\tilde{\lambda}$ and $\tilde{\kappa}$ are compression index and swell index, respectively.

3. Numerical implementation

3.1. Discretization in space

The equation of motion (33) is discretized in space by an updated Lagrangian meshfree scheme. In this method, a porous continuum material is discretized into a finite number of mixed material points (i.e., solid skeleton and pore water). Under the assumption of drained conditions, each material point has one kind of degree of freedom (i.e., displacement) because the negative pore water pressure (matric suction) is constant at each individual material point under drained conditions (i.e., one-way coupling). The uniform grid is used to spatially discretize the problem domain in which all material points have an identical size. Fig. 3 provides a flowchart of the global solution

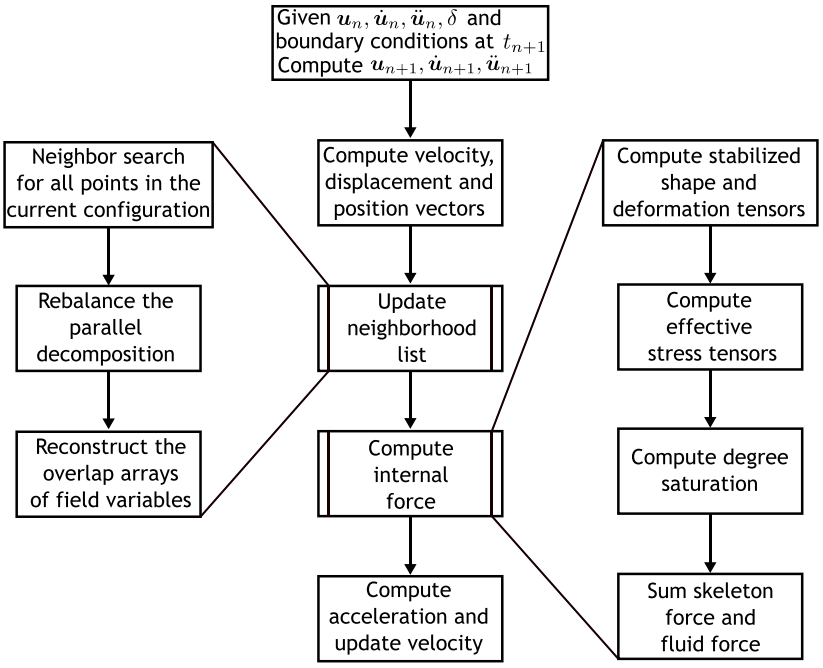

Fig. 3. Global flowchart for the explicit numerical algorithm for the updated Lagrangian peripheromechanics.

procedure and Algorithm 1 summarizes the detailed steps for updating the total force states (i.e., effective force and fluid force states) at load step $n+1$ from time step n. At time step n the material points in the family of a material point are updated through a search algorithm and the neighboring material points are described by their material coordinates (i.e., Lagrangian). At time step $n+1$, calculations of all variables (e.g., sub-horizon, deformation gradient, velocity gradient) are referred to the configuration of solid skeleton at time step n (i.e., updated Lagrangian formulation) instead of the initial/undeformed configuration of solid skeleton (i.e., total Lagrangian formulation).

Let $\mathcal{P}$ denote the number of total material points in the problem domain and $\mathcal{N}_i$ be the number of material points in the horizon of material point i. The spatially discretized equation of motion can be written as

$$\mathscr{A}_{i=1}^{\mathcal{P}}(\boldsymbol{\mathcal{M}}_i\ddot{\boldsymbol{u}}_i - \overline{\boldsymbol{\mathcal{T}}}_i + \boldsymbol{\mathcal{T}}_{w,i} + \boldsymbol{\mathcal{F}}_i) = 0, \tag{47}$$

where $\mathscr{A}$ is a global linear assembly operator [4,69], $\boldsymbol{\mathcal{M}}_i$ is the mass matrix at material point i, $\overline{\boldsymbol{\mathcal{T}}}_i$ is the vector of effective force, $\boldsymbol{\mathcal{T}}_{w,i}$ is the vector of fluid force and $\boldsymbol{\mathcal{F}}_i$ is the vector of gravity force. In the current configuration of solid skeleton, the three variables can be written as

$$\boldsymbol{\mathcal{M}}_i = \left[\rho_s(1-\phi_i) + \rho_w S_{r,i}\phi_i\right]\mathscr{V}_i\mathbf{1}, \tag{48}$$

$$\overline{\boldsymbol{\mathcal{T}}}_i = \sum_{j=1}^{\mathcal{N}_i}\left(\underline{\overline{\boldsymbol{\mathcal{T}}}}_{(ij)} - \underline{\overline{\boldsymbol{\mathcal{T}}}}_{(ji)}\right)\mathscr{V}_j\mathscr{V}_i, \tag{49}$$

$$\boldsymbol{\mathcal{T}}_{w,i} = \sum_{j=1}^{\mathcal{N}_i}\left(S_{r,i}\underline{\boldsymbol{\mathcal{T}}}_{w,(ij)} - S_{r,j}\underline{\boldsymbol{\mathcal{T}}}_{w,(ji)}\right)\mathscr{V}_j\mathscr{V}_i, \tag{50}$$

where $\mathscr{V}_i$ and $\mathscr{V}_j$ are the volumes of material points i and j, respectively, in the current configuration.

In (49) and (50), the effective force state and the water force state are written as

$$\underline{\overline{\boldsymbol{\mathcal{T}}}}_{(ij)} = \varpi_{(ij)}\underline{\omega}_{(ij)}\underline{\boldsymbol{\zeta}}_{(ij)}\boldsymbol{\mathcal{K}}^{-1}_{(ij)}\overline{\boldsymbol{\sigma}}_{(ij)}, \tag{51}$$

$$\underline{\overline{\boldsymbol{\mathcal{T}}}}_{(ji)} = \varpi_{(ji)}\underline{\omega}_{(ji)}\underline{\boldsymbol{\zeta}}_{(ji)}\boldsymbol{\mathcal{K}}^{-1}_{(ji)}\overline{\boldsymbol{\sigma}}_{(ji)}, \tag{52}$$

$$\underline{\boldsymbol{\mathcal{T}}}_{(w,ij)} = \varpi_{(ij)}\underline{\omega}_{(ij)}\underline{\boldsymbol{\zeta}}_{(ij)}\boldsymbol{\mathcal{K}}^{-1}_{(ij)}\mathbf{1}p_{w,i}, \tag{53}$$

$$\underline{\mathscr{T}}_{(w,ji)} = \varpi_{(ji)}\underline{\omega}_{(ji)}\underline{\boldsymbol{\zeta}}_{(ji)}\boldsymbol{\mathscr{K}}^{-1}_{(ji)}\mathbf{1}p_{w,j}. \tag{54}$$

The weighting factors $\varpi_{(ij)}$ and $\varpi_{(ij)}$ in (51)–(54) are defined as

$$\varpi_{(ij)} = \frac{\sum_{k=1}^{\mathcal{N}_{(ij)}} \mathscr{V}_k}{\sum_{l=1}^{\mathcal{N}_i} \mathscr{V}_l}, \tag{55}$$

$$\varpi_{(ji)} = \frac{\sum_{k=1}^{\mathcal{N}_{(ji)}} \mathscr{V}_k}{\sum_{l=1}^{\mathcal{N}_j} \mathscr{V}_l}, \tag{56}$$

where $\mathcal{N}_{(ij)}$ is the number of material points in the sub-horizon $\mathscr{H}_{(ij)}$ and $\mathcal{N}_{(ji)}$ is the number of material points in the sub-horizon $\mathscr{H}_{(ji)}$. Note that for the case of $\delta = \delta'$, $\mathcal{N}_{(ij)} = \mathcal{N}_{(ji)}$.

The velocity gradient is written as

$$\boldsymbol{\mathscr{L}}_{(ij)} = \left[\sum_{k=1}^{\mathcal{N}_{(ij)}} \left(\underline{\omega}_{(ij)}\dot{\boldsymbol{\mathscr{Y}}}_{(ik)} \otimes \underline{\boldsymbol{\zeta}}_{(ik)}\right) \mathscr{V}_k\right] (\boldsymbol{\mathscr{K}}_{(ij)})^{-1}. \tag{57}$$

The rate of deformation tensor reads

$$\boldsymbol{\mathscr{D}}_{(ij)} = \frac{1}{2}\left[\boldsymbol{\mathscr{L}}_{(ij)} + \boldsymbol{\mathscr{L}}_{(ji)}\right]. \tag{58}$$

Then the increment in strain reads

$$\Delta\boldsymbol{\varepsilon}_{(ij)} = \Delta t\ \boldsymbol{\mathscr{D}}_{(ij)}. \tag{59}$$

Given (59) a classical constitutive model for unsaturated porous media can be used to compute $\overline{\boldsymbol{\sigma}}_{(ij)}$ as described in Section 3.2.1. Next, we introduce the temporal discretization through an explicit Newmark scheme.

3.2. Integration in time

The Newmark scheme [69] is adopted to integrate the motion of equation in time. Let $\boldsymbol{u}_n, \dot{\boldsymbol{u}}_n$ and $\ddot{\boldsymbol{u}}_n$ be the displacement, velocity, and acceleration vectors at time step n. The predictors of displacement and velocity in a general Newmark scheme read

$$\tilde{\dot{\boldsymbol{u}}}_{n+1} = \dot{\boldsymbol{u}}_n + (1-\beta_1)\Delta\ddot{\boldsymbol{u}}_n, \tag{60}$$

$$\tilde{\boldsymbol{u}}_{n+1} = \boldsymbol{u}_n + \Delta t\dot{\boldsymbol{u}}_n + \frac{\Delta t^2}{2}(1-2\beta_2)\,\ddot{\boldsymbol{u}}_n, \tag{61}$$

where β_1 and β_2 are numerical integration parameters. Given (60) and (61), the acceleration $\boldsymbol{a}_{n+1}$ is determined by the recursion relation

$$\ddot{\boldsymbol{u}}_{n+1} = \boldsymbol{\mathscr{M}}^{-1}_{n+1}(\boldsymbol{\mathcal{F}}_{n+1} - \widetilde{\overline{\boldsymbol{\mathscr{T}}}}_{n+1} + \widetilde{\boldsymbol{\mathscr{T}}}_{w,n+1}), \tag{62}$$

where $\widetilde{\overline{\boldsymbol{\mathscr{T}}}}_{n+1}$ and $\widetilde{\boldsymbol{\mathscr{T}}}_{w,n+1}$ are determined from (61) and the local constitutive model. From (62), the displacement and velocity at time step $n+1$ can be updated as

$$\dot{\boldsymbol{u}}_{n+1} = \tilde{\dot{\boldsymbol{u}}}_{n+1} + \beta_1\Delta t\ddot{\boldsymbol{u}}_{n+1}, \tag{63}$$

$$\boldsymbol{u}_{n+1} = \tilde{\boldsymbol{u}}_{n+1} + \beta_2\Delta t^2\ddot{\boldsymbol{u}}_{n+1}. \tag{64}$$

In this study, we adopt the explicit central difference solution scheme [69] in which $\beta_1 = 1/2$ and $\beta_2 = 0$. We note that the explicit method is efficient and robust to model dynamic problems with extreme large deformation [26]. Fig. 4 plots a flowchart of the algorithm and Algorithm 2 summarizes the central difference time integration scheme.

For the numerical stability of the explicit algorithm, the critical time step is determined through a simple method originally formulated for the bond-based peridynamics for solids (e.g., [26])

$$\Delta t_c = \sqrt{\frac{2(1-\phi)\rho_s}{\sum_j^{\mathcal{N}_i} \mathscr{V}_j \mathcal{C}|\boldsymbol{\zeta}_{(ij)}|}}, \tag{65}$$

Algorithm 1 Given $\boldsymbol{u}$ construct effective force vector $\overline{\boldsymbol{\mathcal{T}}}$ and pressure force vector $\boldsymbol{\mathcal{T}}_w$

Execute neighbor search: $\forall j \in \mathcal{B}$, if $|\underline{\boldsymbol{\zeta}}_{(ij)}| \leq \delta_i$ add j to the neighbor list of i, the set $\mathcal{H}_i$
for all points i **do**
  for all neighboring points j **do**
    Search for the sub-horizon neighbors: $\forall k \in \mathcal{H}_i$, if $|\underline{\boldsymbol{\zeta}}_{jk}| \leq \delta_j$, then $k \in \mathcal{H}_{(ij)}$
    for all sub-horizon neighbors k **do**
      Compute contribution of bond ik to the shape tensor $\boldsymbol{\mathcal{K}}_{(ij)}$ using (23)
    end for
    Compute the sub-horizon based deformation gradient $\boldsymbol{\mathcal{F}}_{(ij)}$ using (24)
  end for
  Compute deformation gradient $\boldsymbol{\mathcal{F}}_i$ and its determinant $\mathcal{J}_i$ using (17)
end for
for all points i **do**
  for all neighboring points j **do**
    for all sub-horizon neighbors k **do**
      Compute the contribution of bond ik to the velocity gradient $\boldsymbol{\mathcal{L}}_{(ij)}$ using (25)
    end for
    Compute the rate of deformation $\boldsymbol{\mathcal{D}}_{(ij)}$ using (26)
    Compute the strain increment using (59)
    Compute Cauchy stress $\overline{\boldsymbol{\sigma}}_{(ij)}$
  end for
  Compute the degree of saturation S_r using (15)
end for
for all points i **do**
  for all neighboring points j **do**
    Compute $\overline{\boldsymbol{\mathcal{T}}}_{(ij)}$ using (51)
    Compute $\boldsymbol{\mathcal{T}}_{w,ij}$ using (53)
  end for
end for
for all points i **do**
  Compute $\overline{\boldsymbol{\mathcal{T}}}_i$ using (49)
  Compute $\boldsymbol{\mathcal{T}}_{w,i}$ using (50)
end for

where ϕ is the porosity and ρ_s is the intrinsic density of solid skeleton as defined previously, and $\mathcal{C}_{ij}$ is the micro-mechanical elastic modulus for a bond ij [5,26]. We note that (65) can provide a conservative estimate for state-based peridynamics [70]. However, for the extreme large deformation analysis involving visco-plasticity and contact the numerical instability could occur even when (65) is followed. Thus we perform an energy balance check to ensure stability of the algorithm. The internal energy, external energy and kinetic energy of the system at time step $n+1$ can be written as

$$\mathcal{W}_{\text{int},n+1} = \mathcal{W}_{\text{int},n} + \frac{\Delta t}{2}\left(\dot{\boldsymbol{u}}_n + \frac{1}{2}\Delta t\ddot{\boldsymbol{u}}_n\right)\left[\left(\overline{\boldsymbol{\mathcal{T}}}_n - \boldsymbol{\mathcal{T}}_{w,n}\right) + \left(\overline{\boldsymbol{\mathcal{T}}}_{n+1} - \boldsymbol{\mathcal{T}}_{w,n+1}\right)\right], \tag{66}$$

$$\mathcal{W}_{\text{ext},n+1} = \mathcal{W}_{\text{ext},n} + \frac{\Delta t}{2}\left(\dot{\boldsymbol{u}}_n + \frac{1}{2}\Delta t\ddot{\boldsymbol{u}}_n\right)\left(\boldsymbol{\mathcal{F}}_n + \boldsymbol{\mathcal{F}}_{n+1}\right), \tag{67}$$

$$\mathcal{W}_{\text{kin},n+1} = \frac{1}{2}\dot{\boldsymbol{u}}_{n+1}\boldsymbol{\mathcal{M}}_{n+1}\dot{\boldsymbol{u}}_{n+1}. \tag{68}$$

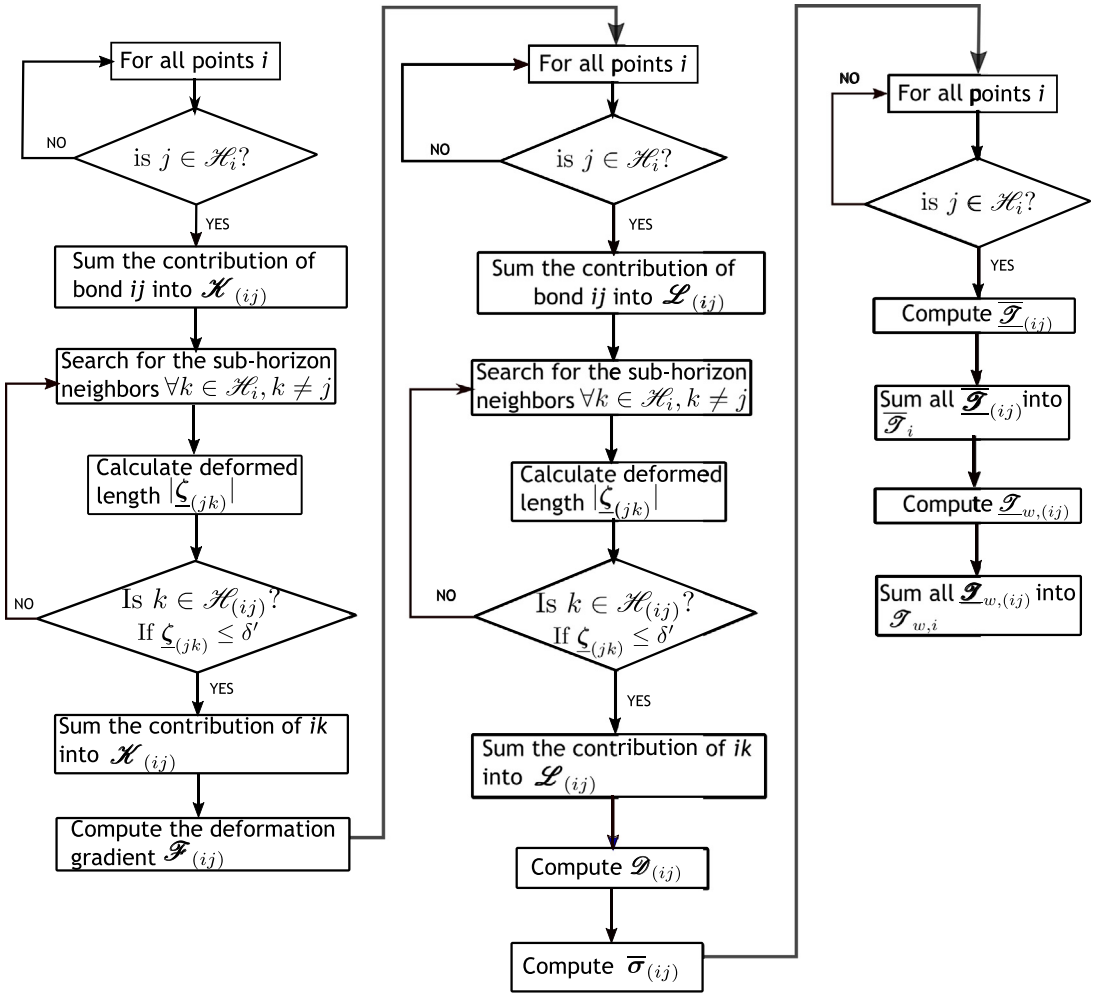

Fig. 4. Flowchart for the computation at the material point level for the sub-horizon based updated Lagrangian peridynamics.

Then energy conservation requires that

$$|\mathscr{W}_{\text{int},n+1} + \mathscr{W}_{\text{kin},n+1} - \mathscr{W}_{\text{ext},n+1}| \leq \bar{\varepsilon} \max(\mathscr{W}_{\text{kin},n+1}, \mathscr{W}_{\text{int},n+1}, \mathscr{W}_{\text{ext},n+1}), \tag{69}$$

where $\bar{\varepsilon}$ is a small tolerance on the order of 10^{-2} [21].

For self completeness, in what follows we summarize the numerical integration algorithm for the local constitutive model.

3.2.1. Integration of the local constitutive model

The backward Euler integration scheme is adopted to numerically implement the adopted viscoplasticity model for unsaturated soil in the updated Lagrangian peridynamics model (e.g., [1]). Given $\Delta\boldsymbol{\varepsilon}_{n+1} = \boldsymbol{\varepsilon}_{n+1} - \boldsymbol{\varepsilon}_n$, the trial effective stress tensor can be computed from the elastic model. For the elastic loading case, the trial effective stress tensor is the real effective stress. For the visco-plastic loading case (i.e., $f > 0$), the effective stress and effective apparent pre-consolidation pressure can be solved in the stress invariant $(\overline{p}, q)$ space as follows. At time step $n+1$, $\overline{p}$, q, and p_c can be written as

$$\overline{p} = \overline{p}^{tr} - K \frac{f \Delta t}{\eta} \left(\frac{\partial f}{\partial \overline{p}} \right), \tag{70}$$

Algorithm 2 Explicit Newmark time integration scheme

1: Set initial conditions $\dot{\boldsymbol{u}}_0$, $\boldsymbol{u} = 0$, $t_n = 0$, $\overline{\boldsymbol{\sigma}}_0$, $\boldsymbol{p}_{w0}$ and compute $\Delta t = \Delta t_{crit}$ using (65)
2: Evaluate initial state using Algorithm 1
3: Compute initial acceleration $\ddot{\boldsymbol{u}}_0 = \boldsymbol{\mathscr{M}}_0^{-1}(-\overline{\boldsymbol{\mathscr{T}}}_0 + \boldsymbol{\mathscr{T}}_{w,0})$
4: **while** $t_n < t_{\text{final}}$ **do**
5: Update time $t_{n+1} = t_n + \Delta t$
6: Compute the predictor $\tilde{\ddot{\boldsymbol{u}}}_{n+1}$ using (60)
7: Apply boundary conditions
8: Compute the displacement $\boldsymbol{u}_{n+1}$ using (64)
9: Compute internal force using Algorithm 1
10: Compute the acceleration $\ddot{\boldsymbol{u}}_{n+1}$ using (62)
11: Compute the velocity $\dot{\boldsymbol{u}}_{n+1}$ using (63)
12: Compute global kinetic energy $\mathscr{W}_{\text{kin},n+1}$, internal energy $\mathscr{W}_{\text{int},n+1}$ and external energy $\mathscr{W}_{\text{ext},n+1}$ using (66), (67) and (68), respectively
13: Check energy balance using (69)
14: $n \leftarrow n + 1$
15: **end while**
16: **end**

$$q = q^{tr} - 3\mu_s \frac{f\,\Delta t}{\eta}\left(\frac{\partial f}{\partial q}\right), \tag{71}$$

$$p_c = p_{c,n} \exp\left[\frac{f\,\Delta t}{(\tilde{\lambda} - \tilde{\kappa})\eta}\left(\frac{\partial f}{\partial \overline{p}}\right)\right]. \tag{72}$$

The values of $\overline{p}, q, p_c$ at time step $n+1$ can be determined through Newton's method by defining a residual vector $\boldsymbol{r} = \{r_1, r_2, r_3\}^T$ as

$$r_1 = \overline{p} - \overline{p}^{tr} + K\frac{f\,\Delta t}{\eta}\left(\frac{\partial f}{\partial \overline{p}}\right), \tag{73}$$

$$r_2 = q - q^{tr} + 3\mu_s \frac{f\,\Delta t}{\eta}\left(\frac{\partial f}{\partial q}\right), \tag{74}$$

$$r_3 = p_c - p_{c,n} \exp\left[\frac{f\,\Delta t}{(\tilde{\lambda} - \tilde{\kappa})\eta}\left(\frac{\partial f}{\partial \overline{p}}\right)\right], \tag{75}$$

where $\overline{p}^{\text{tr}}$ and q^{tr} are the trial values by freezing the viscoplastic deformation at time step $n+1$ [65]. Let the local unknown vector be $\boldsymbol{x} = \{\overline{p}, q, p_c\}^T$, through Newton's method $\boldsymbol{x}$ can be solved as

$$\boldsymbol{x}^{k+1} = \boldsymbol{x}^k - \boldsymbol{A}^{-1}\boldsymbol{r}^k(\boldsymbol{x}), \tag{76}$$

where k is the iteration counter and $\boldsymbol{A}$ is the local tangent operator that reads

$$\boldsymbol{A} = \begin{bmatrix} A_{11} & A_{12} & A_{13} \\ A_{21} & A_{22} & A_{23} \\ A_{31} & A_{32} & A_{33} \end{bmatrix}. \tag{77}$$

The elements of $\boldsymbol{A}$ can be obtained by chain rule as

$$A_{11} = 1 + K\frac{\Delta t}{\eta}\left[\left(\frac{\partial f}{\partial \overline{p}}\right)^2 + f\frac{\partial^2 f}{\partial \overline{p}^2}\right], \tag{78}$$

$$A_{12} = K\frac{\Delta t}{\eta}\left(\frac{\partial f}{\partial \overline{p}}\frac{\partial f}{\partial q}\right), \tag{79}$$

$$A_{13} = K\frac{\Delta t}{\eta}\left(\frac{\partial f}{\partial \overline{p}}\frac{\partial f}{\partial \overline{p}_c} + f\frac{\partial^2 f}{\partial \overline{p}\partial \overline{p}_c}\right)\frac{\partial \overline{p}_c}{\partial p_c}, \tag{80}$$

$$A_{21} = 3\mu_s \frac{\Delta t}{\eta}\left(\frac{\partial f}{\partial q}\frac{\partial f}{\partial \overline{p}}\right), \tag{81}$$

$$A_{22} = 1 + 3\mu_s \frac{\Delta t}{\eta}\left[f\frac{\partial^2 f}{\partial q^2} + \left(\frac{\partial f}{\partial q}\right)^2\right], \tag{82}$$

$$A_{23} = 3\mu_s \frac{\Delta t}{\eta}\left(\frac{\partial f}{\partial q}\frac{\partial f}{\partial \overline{p}_c}\right)\frac{\partial \overline{p}_c}{\partial p_c}, \tag{83}$$

$$A_{31} = -p_c \frac{\Delta t}{(\tilde{\lambda}-\tilde{\kappa})\eta}\left[\left(\frac{\partial f}{\partial \overline{p}}\right)^2 + f\frac{\partial^2 f}{\partial \overline{p}^2}\right], \tag{84}$$

$$A_{32} = -p_c \frac{\Delta t}{(\tilde{\lambda}-\tilde{\kappa})\eta}\left(\frac{\partial f}{\partial \overline{p}}\frac{\partial f}{\partial q}\right), \tag{85}$$

$$A_{33} = 1 - p_c \frac{\Delta t}{(\tilde{\lambda}-\tilde{\kappa})\eta}\left(\frac{\partial f}{\partial \overline{p}}\frac{\partial f}{\partial \overline{p}_c} + f\frac{\partial^2 f}{\partial \overline{p}\partial \overline{p}_c}\right)\frac{\partial \overline{p}_c}{\partial p_c}, \tag{86}$$

where

$$\frac{\partial f}{\partial \overline{p}} = 2\overline{p} - \overline{p}_c, \tag{87}$$

$$\frac{\partial^2 f}{\partial \overline{p}^2} = 2, \tag{88}$$

$$\frac{\partial f}{\partial q} = 2q/M^2, \tag{89}$$

$$\frac{\partial f}{\partial \overline{p}_c} = -\overline{p}, \tag{90}$$

$$\frac{\partial^2 f}{\partial \overline{p}\partial \overline{p}_c} = -1, \tag{91}$$

$$\frac{\partial^2 f}{\partial q^2} = 2/M^2, \tag{92}$$

$$\frac{\partial \overline{p}_c}{\partial p_c} = b_2 \exp(b_1)(-p_c)^{b_2-1}. \tag{93}$$

$$\tag{94}$$

4. Numerical examples

In this section, we present two numerical examples to demonstrate the stability and efficacy of the updated Lagrangian peripоromechanics paradigm for modeling extreme large deformation in unsaturated porous media. In example 1, we conduct a uniaxial compression test of a two-dimensional soil specimen to demonstrate the stability of the updated Lagrangian peripоromechanics paradigm under static and dynamic conditions. In example 2, we model the unsaturated soil column collapse that involves extreme large deformation. In example 2, the numerical results are compared against the experimental data under dry conditions in the literature. Then we study the impact of initial matric suction and substrate roughness on the soil column collapse. We note that the soil column collapse is adopted as a numerical example in this study because it is a significant problem related to geo-hazard engineering (e.g., landslides and debris flow) that involves extreme large deformation in geomaterials. In this study the boundary layer method is adopted to impose boundary conditions in the implemented numerical model (e.g., [4,13]).

4.1. Uniaxial compression test

This example deals with the stability analysis of the sub-horizon based updated Lagrangian peripоromechanics model. The stability analysis is focused on the correspondence principle formulated in the updated Lagrangian peripоromechanics model. We note that in poromechanics the values of parameters like the permeability, fluid viscosity, and the degree of saturation may affect the stability which are not investigated here. We simulate the

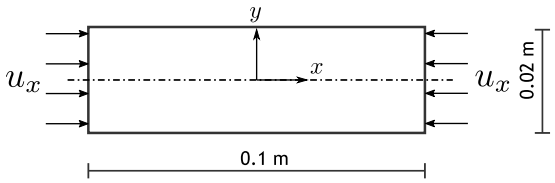

Fig. 5. Problem setup for the uniaxial compression test.

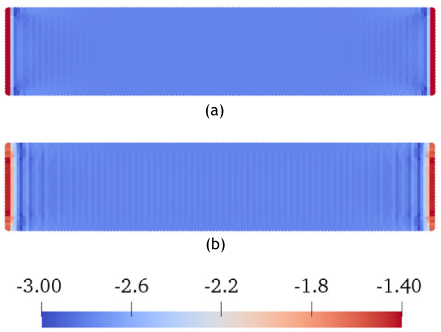

Fig. 6. Contours of $\overline{\sigma}_x$ ($\times$ 100 kPa) from the quasi-static simulations using the original correspondence elastic constitutive model with (a) $m = 2$ and (b) $m = 3$ at $u_x = 0.5 \times 10^{-3}$ m.

uniaxial compression of a rectangular specimen with zero matric suction under quasi-static and dynamic conditions. Note that for the quasi-static case an implicit time integration scheme [4] is utilized. The problem geometry and loading protocol are presented in Fig. 5. The problem is discretized into 12,000 uniform material points. The distance between two adjacent material point centers is $\Delta = 0.005$ m. An isotropic elastic correspondence constitutive model is utilized for the solid skeleton. The material parameters adopted are bulk modulus $K = 25$ MPa, shear modulus $\mu_s = 15$ MPa, solid skeleton density $\rho_s = 2200$ kg/m^3 and initial porosity $\phi = 0.2$. The simulation is repeated using two horizons, i.e., $\delta_1 = 0.01$ m and $\delta_2 = 0.015$ m. The ratios of δ/Δ are $m = 2$ and $m = 3$, respectively.

The total applied displacement is $u_x = 0.5 \times 10^{-3}$ m. The total loading time is $t = 0.1$ s. The time increment for the quasi-static simulation is $\Delta t_1 = 0.001$ s and the time increment for the dynamic loading case is $\Delta t_2 = 3\times10^{-6}$ s that meets the critical time step criterion. The numerical results are presented in Figs. 6–11. For clarity, in what follows the stabilized correspondence constitutive model means that the local constitutive model for porous media is implemented using the sub-horizon based correspondence principle formulated in this study. The standard correspondence constitutive model means that the local constitutive model for porous media is implemented using the original multiphase correspondence principle [2,14].

Fig. 6 presents the contours of $\overline{\sigma}_x$ from the simulations through the standard correspondence constitutive model with two values of m. For comparison, Fig. 7 plots the contours of $\overline{\sigma}_x$ from the simulations using the stabilized correspondence constitutive model. The contours of $\overline{\sigma}_x$ in Fig. 6 show noticeable oscillations. Fig. 7 shows that the oscillations have disappeared in the results with the stabilized correspondence constitutive model.

Fig. 8 compares the variations of $\overline{\sigma}_x$ along the x axis of the specimen from the simulations with stabilized and standard correspondence material models. The results show that the higher value of m produces larger oscillations in $\overline{\sigma}_x$ from the simulations using the standard correspondence constitutive model. For the simulations using the stabilized correspondence constitutive model the oscillations have been eliminated for both values of m ratios.

Figs. 9 and 10 present the contours of $\overline{\sigma}_x$ from the dynamic simulations with two values of m using the standard and stabilized correspondence constitutive models, respectively. Fig. 11 compares the variations of $\overline{\sigma}_x$ along the x axis of the specimen. It is found that the numerical instabilities in the simulations with the standard correspondence constitutive models are more noticeable for the dynamic loading case than the static simulations. Overall, the results in both figures show that the simulations with the stabilized correspondence constitutive model eliminates the oscillations in $\overline{\sigma}_x$.

Finally, for a convergence analysis we re-run the simulations in the dynamic loading cases with stabilized updated Lagrangian peridynamics using three spatial discretization schemes. The three spatial discretization schemes

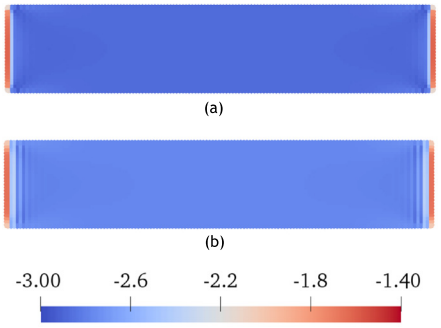

Fig. 7. Contours of $\overline{\sigma}_x$ ($\times$ 100 kPa) from the quasi-static simulations using the stabilized correspondence constitutive model with (a) $m = 2$ and (b) $m = 3$ at $u_x = 0.5 \times 10^{-3}$ m.

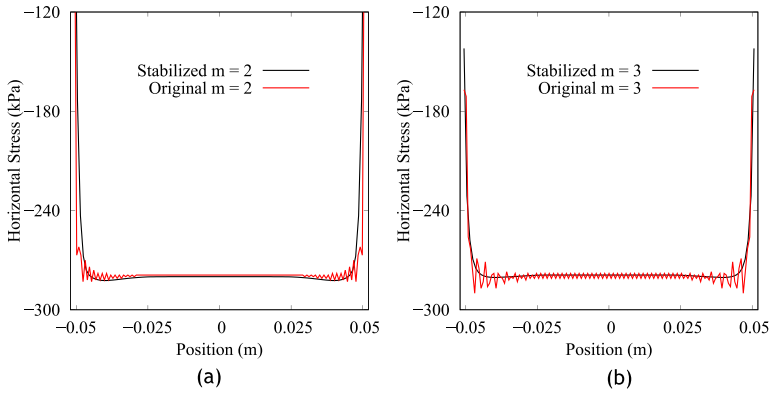

Fig. 8. Comparison of $\overline{\sigma}_x$ along the x axis of the specimen from the static loading case with (a) $m = 2$ and (b) $m = 3$.

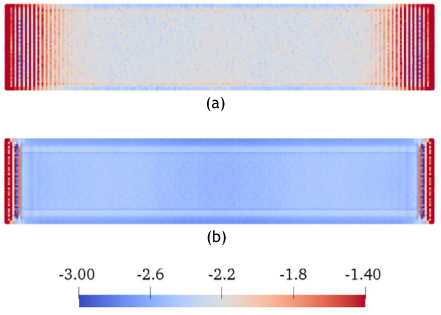

Fig. 9. Contours of $\overline{\sigma}_x$ ($\times$ 100 kPa) from the dynamic loading case with (a) m = 2 and (b) m = 3 using the original correspondence constitutive model.

consist of 15,000, 30,000 and 50,000 material points, respectively. The results are shown in Figs. 12 and 13. Fig. 12 presents the contours of $\overline{\sigma}_x$ of the simulations with three spatial discretization schemes at u_x = 0.001 m. Fig. 13 presents the variations of $\overline{\sigma}_x$ along the x axis for the three cases at u_x = 0.001 m. The results in Figs. 12 and 13 demonstrate that the numerical results with the three spatial discretization schemes agree well with each other. This agreement implies that the numerical solution is unique.

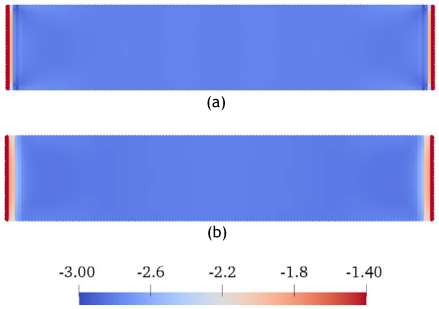

Fig. 10. Contours of $\overline{\sigma}_x$ ($\times$ 100 kPa) from the dynamic loading case with (a) m = 2 and (b) m = 3 using the stabilized correspondence constitutive model.

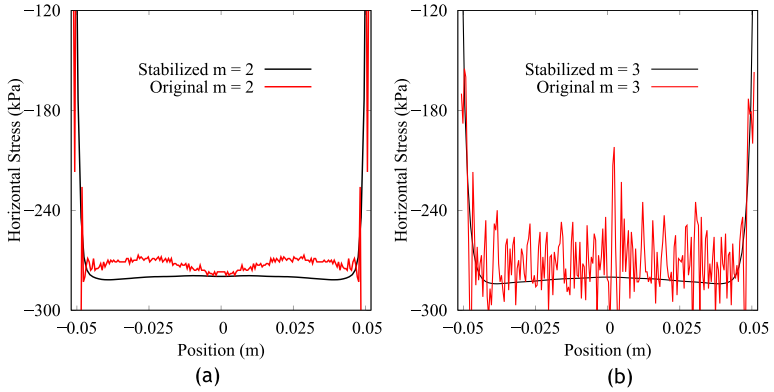

Fig. 11. Comparison of $\overline{\sigma}_x$ along the x axis of the specimen from the dynamic loading case with (a) m=2 and (b) m = 3.

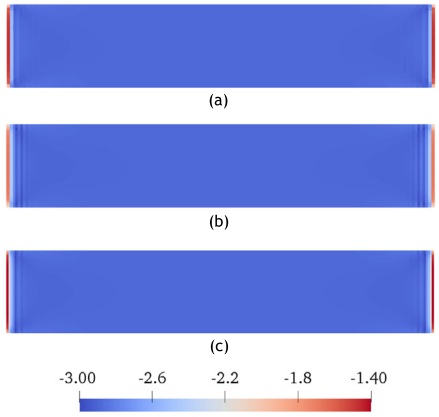

Fig. 12. Comparison of contours of $\overline{\sigma}_x$ ($\times$ 100 kPa) with the three spatial discretization schemes (a) case 1 = 15,000 (material points), (b) case 2 = 30,000, and (c) case 3 = 50,000 at u_x = 0.001 m.

4.2. Unsaturated soil column collapse in two dimensions

In this example, through the proposed sub-horizon based updated Lagrangian peridynamics we simulate unsaturated soil column collapse by gravity loading under drained conditions (i.e., one-way coupling) in two dimensions. We first simulate the collapse of a dry column to demonstrate the ability of the formulation to model extreme large plastic deformation in porous media. We then investigate the influence of the aspect ratio, initial matric suction and sub-grade roughness on the characteristics of collapse. All the simulations are conducted using

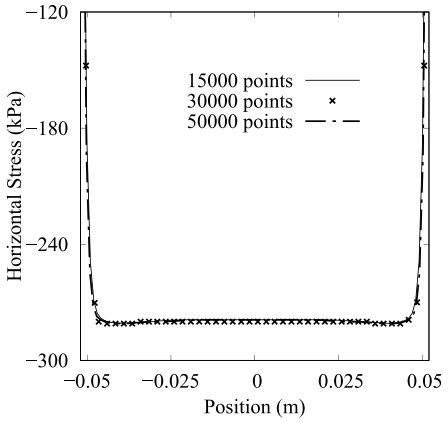

Fig. 13. Comparison of $\overline{\sigma}_x$ along the x axis of the specimen from the simulations with the three spatial discretization schemes at u_x = 0.001 m.

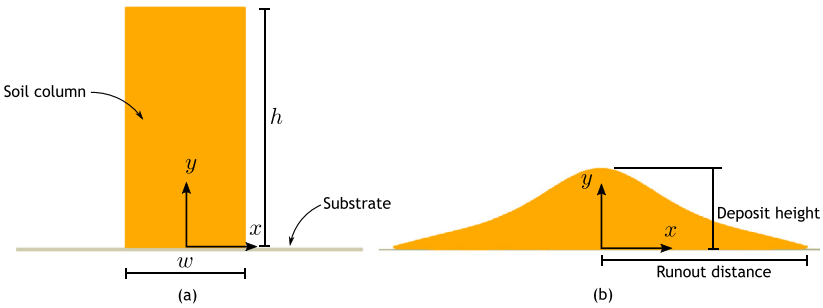

Fig. 14. Problem setup for unsaturated soil column collapse in two-dimensions (a) initial configuration, (b) final configuration.

64 CPU (central processing unit) cores with a total 512 GB (gigabyte) of dedicated memory. Next, we introduce the problem set up, input material parameters, initial conditions, and the contact model for the soil column and the rigid substrate.

The problem geometry is depicted in Fig. 14. The solid skeleton is modeled using the visco-plastic constitutive model introduced in Section 3.2.1. The rigid substrate is modeled using an isotropic elastic model. For the solid skeleton the material parameters are: K = 25 MPa, μ_s = 15 MPa, ρ_s = 2200 kg/m^3, ρ_w = 1000 kg/m^3, initial porosity $\phi = 0.2$, $M = 1.1$, $\tilde{\lambda} = 0.12$, $\tilde{\kappa} = 0.04$, $\eta = 1000$ Pa^3/s and an over-consolidation ratio of 1.25 (i.e., slightly overconsolidated soil). The parameters for the soil–water retention curve are: $\alpha_1 = 0.038$, $\alpha_2 = 3.49$ and $\alpha_3 = 1.25$. The initial geostatic stress in the soil is prescribed through a quasi-static loading step. Subsequently, the lateral constraints on the soil column are relaxed to allow it to collapse onto the rigid substrate.

A contact model for the interface of the soil and the substrate is needed to model the spreading of soil over the substrate. In this study we adopt the short range force model in [26]. In this contact model, contact interactions are modeled using spring-like repulsive forces acting along the normal to the substrate surface. The contact forces act along virtual bonds that carry only contact force (i.e., no material interaction). The repulsive forces act between pairs of material points within a cut-off distance of each other, δ_c. The repulsive contact force and frictional contact force [71] are defined as

$$\underline{\mathscr{T}}_c = -C_s \left(\delta_c - |\underline{\mathscr{Y}}|\right) \frac{\underline{\mathscr{Y}}}{|\underline{\mathscr{Y}}|}, \tag{95}$$

$$\underline{\mathscr{T}}_f = -\mu_f \ \text{sign}\left(\frac{\partial}{\partial t}|\underline{\mathscr{Y}}|\right) \underline{\mathscr{T}}_c, \tag{96}$$

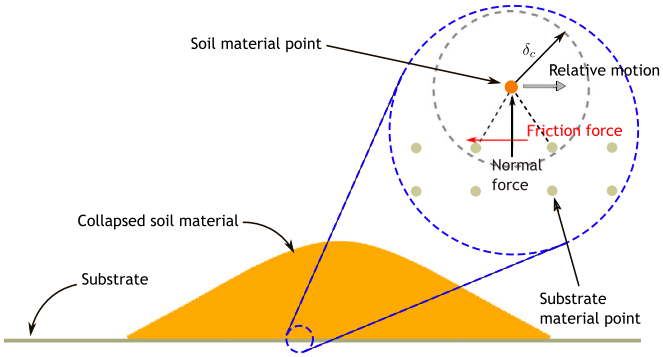

Fig. 15. Schematic of the contact model for the soil column and the substrate.

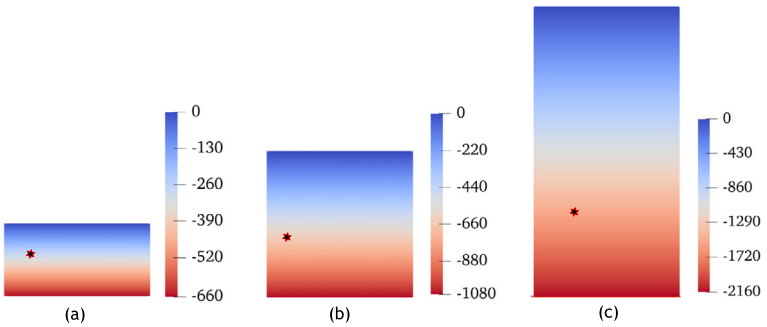

Fig. 16. Contours of initial effective vertical stress $\overline{\sigma}_y$ in the specimens with (a) $a_1 = 2$, (b) $a_2 = 1$ and (c) $a_3 = 0.5$.

where C_s is the contact stiffness and μ_f is the friction coefficient. Given (95) and (96), the equation of motion with the contact model is written as

$$\rho\ddot{\boldsymbol{u}} = \int_{\mathscr{H}_s} (\overline{\underline{\boldsymbol{\mathcal{T}}}} - S_r\underline{\boldsymbol{\mathcal{T}}}_w) - (\overline{\underline{\boldsymbol{\mathcal{T}}}}' - S'_r\underline{\boldsymbol{\mathcal{T}}}'_w)\,\mathrm{d}\mathscr{V}' + \int_{\mathscr{H}_c} \left[(\underline{\boldsymbol{\mathcal{T}}}_c + \underline{\boldsymbol{\mathcal{T}}}_f) - (\underline{\boldsymbol{\mathcal{T}}}'_c + \underline{\boldsymbol{\mathcal{T}}}'_f)\right]\,\mathrm{d}\mathscr{V}' + \boldsymbol{b}, \tag{97}$$

where $\mathscr{H}_c$ is the contact neighborhood defined by δ_c. Fig. 15 depicts the contact interaction between the soil column and the substrate. The initial contact domain is specified in the input file of the numerical model. A search algorithm is used to detect contact pairs in a radius r_c around each individual material point in the defined contact domain. The input parameters for the contact model are: $C_s = 4 \times 10^6$ N/m^2, $\mu_f = 0.25$, $\delta_c = 0.8\Delta$, and $r_c = 3\delta_c$.

In what follows, we study the influence of initial aspect ratios, initial matric suction, and substrate roughness on the soil column collapse.

4.2.1. Influence of initial aspect ratios

We first study the influence of initial aspect ratios (width over height) on the characteristics (e.g., run-out distance and final deposit height) of the soil column collapse under completely dry conditions. Our numerical results are compared with the experimental data in the literature [43,44]. We run the simulations with three aspect ratios, $a_1 = 2$, $a_2 = 1$, and $a_3 = 0.5$. All three specimens have the same initial width w = 0.1 m. Fig. 16 plots the contours of the initial vertical stress in the three specimens.

Figs. 17–19 plot the snapshots of the contours of ε_s for the three aspect ratios. The results show that the aspect ratio could affect the soil column collapse processes and final deposit morphologies which are consistent with the experimental results in the literature [43,44]. As shown in Figs. 17 (a) and 18 for the specimens with $a_1 = 2$ and $a_2 = 1$, banded zone of extensive shear develops during the collapse process. For the specimen with $a_3 = 0.5$, the collapse pattern is clearly different from the simulations using larger aspect ratios. The results confirm the existence of two moving layers observed in the experimental testing. Initially, the contour shows that the upper half of the column moves directly downward with little horizontal movement, while the base rapidly spreads outward.

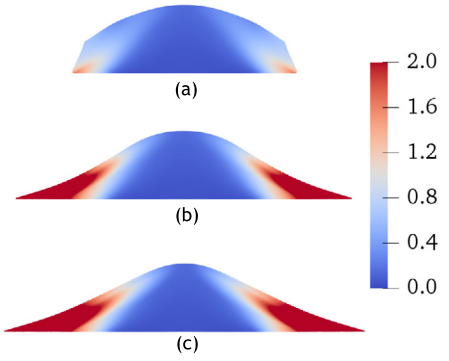

Fig. 17. Contours of ε_s at (a) t = 0.11 s, (b) t = 0.17 s, (c) t = 0.25 s superimposed on the deformed configuration for $a_1 = 2$.

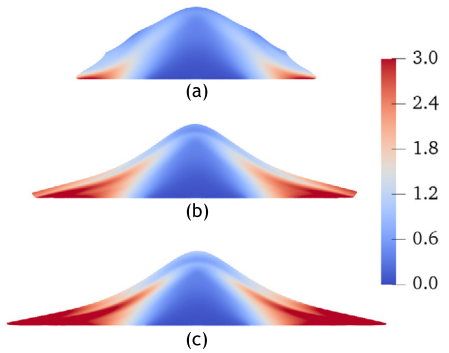

Fig. 18. Contours of ε_s at (a) t = 0.17 s, (b) t = 0.27 s, (c) t = 0.4 s superimposed on the deformed configuration for $a_2 = 1$.

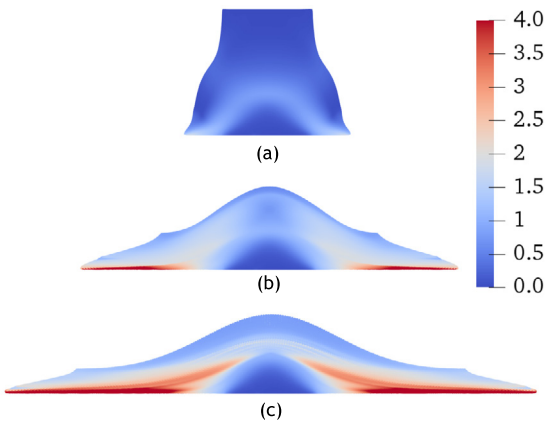

Fig. 19. Contours of ε_s at (a) t = 0.1 s, (b) t = 0.3 s, (c) t = 0.5 s superimposed on the deformed configuration for $a_3 = 0.5$.

Subsequently, the upper half of the column moves laterally and creates two lateral moving fronts, the so-called "Mexican-hat" morphology observed in experimental tests of soil column collapse [43,44]. It is likely that the inertial effects contribute to the change in behavior observed in the simulation with a_3 = 0.5. Figs. 20–22 present the snapshots of the contour of $\overline{\sigma}_y$ for the three aspect ratios. The results show that the aspect ratio could significantly impact the vertical stress states in the final deposit. Both the contours of equivalent shear strains and vertical stresses demonstrate that there could be an underlying and undisturbed region in the soil column throughout the collapse process.

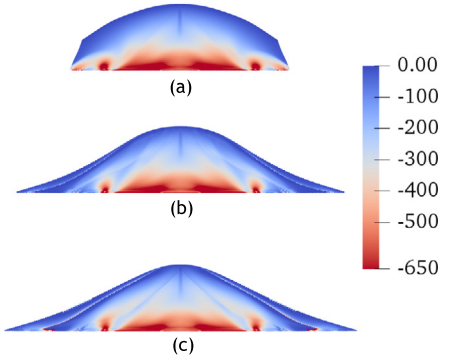

Fig. 20. Contours of $\overline{\sigma}_y$ at (a) t = 0.11 s, (b) t = 0.17 s, (c) t = 0.25 s superimposed on the deformed configuration for $a_1 = 2$.

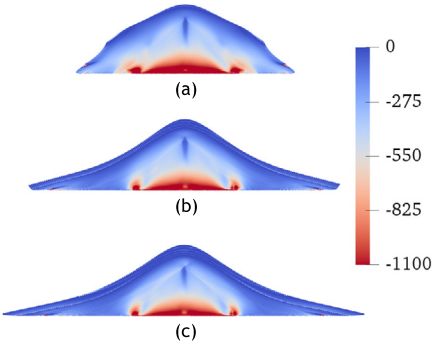

Fig. 21. Contours of $\overline{\sigma}_y$ at (a) t = 0.17 s, (b) t = 0.27 s, (c) t = 0.4 s superimposed on the deformed configuration for $a_2 = 1$.

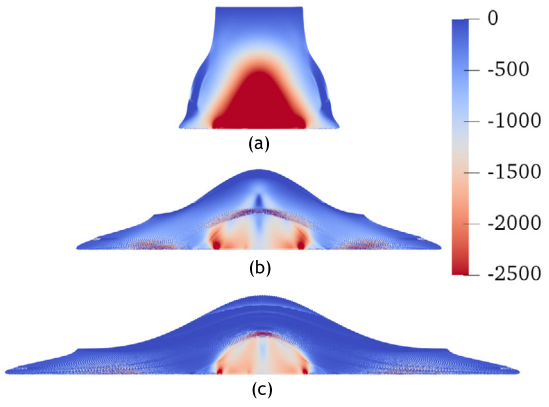

Fig. 22. Contours of $\overline{\sigma}_y$ at (a) t = 0.1 s, (b) t = 0.3 s, (c) t = 0.5 s superimposed on the deformed configuration for $a_3 = 0.5$.

Next, we present the contact force along the base in the final deposit configuration for the simulations with three aspect ratios. Figs. 23 and 24 plot the normal and frictional components of the contact force acting along the base of the final deposit configuration. The results show that both normal and frictional forces along the interface have oscillations along the base of final deposit configurations. The general trend observed from the results in Figs. 23 and 24 is that the normal and shear forces are larger for the specimen with a smaller aspect ratio (i.e., taller soil column).

To validate our numerical results, the final deposit height and runout distance are compared against the experiment testing results in the literature. Here the final runout distance is the distance between the lateral front of the final

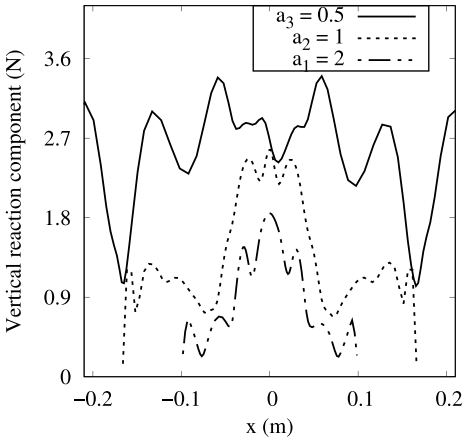

Fig. 23. Variation of the magnitude of the vertical reaction force along the base of the column for 3 aspect ratios.

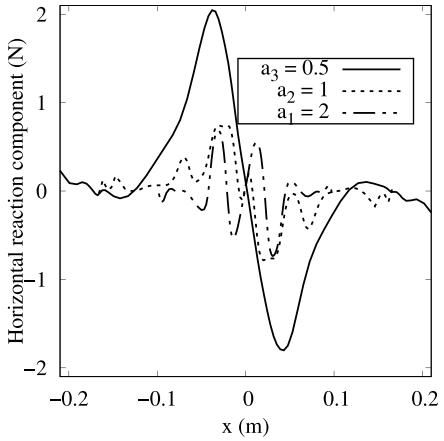

Fig. 24. Variation of the magnitude of the horizontal reaction force along the base of the column for 3 aspect ratios.

deposit and the center along the substrate. The deposit height is measured from the substrate to the highest point of the final deposit. The final height and runout distance are normalized by the initial width of the soil column. Fig. 25 plots the normalized final runout distance from the numerical simulations and the experimental data for three aspect ratios. The numerical results that are consistent with the experimental data demonstrate that the final runout distance decreases with the increase of aspect ratios. Fig. 26 compares the normalized final deposit heights from our numerical simulations and the experimental data for three aspect ratios in the literature. It can be concluded from the results in Figs. 25 and 26 that the update Lagrangian periporomechanics formulation can be applied to model soil column collapse under gravity loading that involves extreme large deformation.

4.2.2. Influence of initial matric suction

The initial matric suction could have a strong impact on the soil collapse process under unsaturated conditions. To test this hypothesis, we run simulations of soil column collapse with three different initial suctions, i.e., $s_1 = 0$ kPa, s_2= 25 kPa, and s_3 = 50 kPa. The corresponding degrees of saturation S_r = 1.0, 0.92 and 0.88 respectively. The simulations are repeated for the above three aspect ratios. All simulations are conducted under drained conditions with a constant matric suction. We note that a constant matric suction is a simplified assumption in that matric suction may not be significant in the extreme deformation regime at the later stage of soil column collapse. The degree of saturation S_r varies with the deformation through the porosity ϕ (i.e., Eq. (15)). In this case, the degree of saturation may decrease with extreme deformation, although a constant matric suction is assumed.

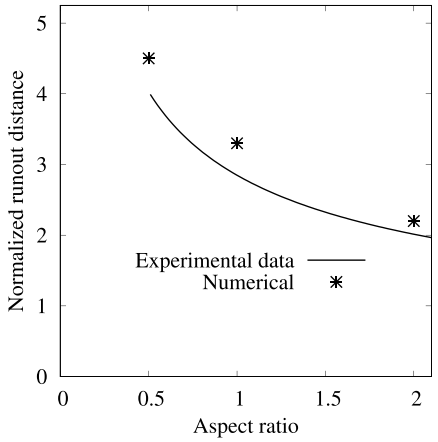

Fig. 25. Comparison of the normalized run-out distance with experimental data [44] for different aspect ratios.

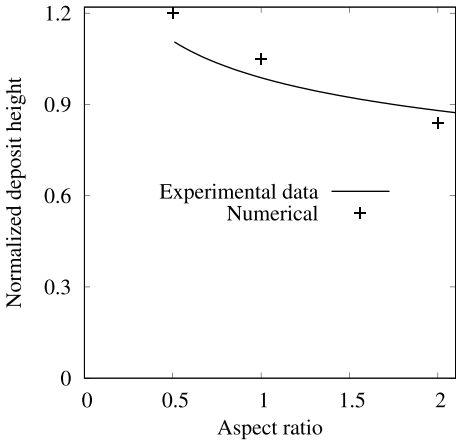

Fig. 26. Comparison of the normalized final deposit height with experimental data [44] for different aspect ratios.

The numerical results are presented in Figs. 27–32. Figs. 27, 28, and 29 plot the snapshots of ε_s in the final deposit configurations from the simulations with three different initial aspect ratios and matric suctions. The results in Figs. 27, 28, and 29 demonstrate that the initial matric suction could significantly affect the final deposit morphology of the soil. The impact of the initial matric suction on the contour of deviatoric strain in the final configuration may depend on the initial aspect ratio of the soil column. For instance, for $a_1 = 2$, as shown in Fig. 27 the initial matric suction affects the maximum deviatoric strain in the soil. However, this influence becomes rather mild when $a_3 = 0.5$ with the same initial column width (i.e., larger initial height of the soil column). Moreover, as shown in Fig. 30 the increase of initial matric suction in the soil column reduces the final runout distance for the same aspect ratio. Under the same initial matric suction, the specimen with the larger aspect ratio generates the smaller final runout distance. The final deposit height is generally larger for the specimen with a larger initial matric suction under the same aspect ratio. These observations can be explained by the fact that increasing matric suction generally increases the cohesion of soils (e.g., [1,72]).

To show the sensitivity of shear strains to initial matric suctions, Fig. 32 plots ε_s over time at the selected material points (see Fig. 16) in the specimens with different aspect ratios. The results in Fig. 32 demonstrate that ε_s is smaller in the specimen with smaller initial matric suction at the same time for $a_1 = 2$ or $a_2 = 1$. For the specimen with $a_3 = 0.5$ the simulation results show similar shear strains in the early stage of the collapse. However, the equivalent shear strain at the same location becomes larger at the later stage of collapse for the larger initial matric suction. It may be concluded that the impact of initial matric suction on collapse could also depend on initial aspect ratios.

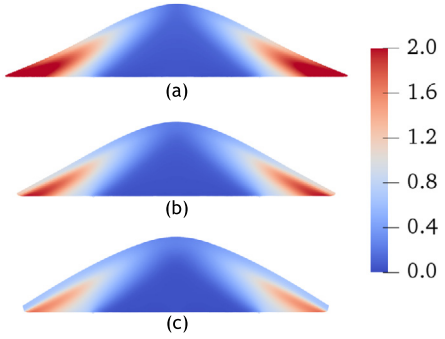

Fig. 27. Contours of ε_s on the final deposit configuration from simulations with (a) s_1 = 0 kPa, (b) s_2 = 25 kPa, and (c) s_3 = 50 kPa for $a_1 = 2$.

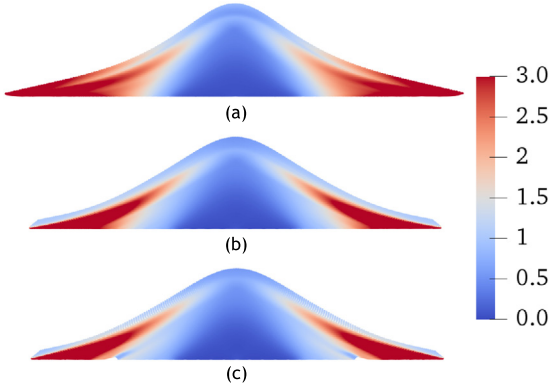

Fig. 28. Contours of ε_s on the final deposit configuration from simulations with (a) s_1 = 0 kPa, (b) s_2 = 25 kPa, and (c) s_3 = 50 kPa for $a_2 = 1$.

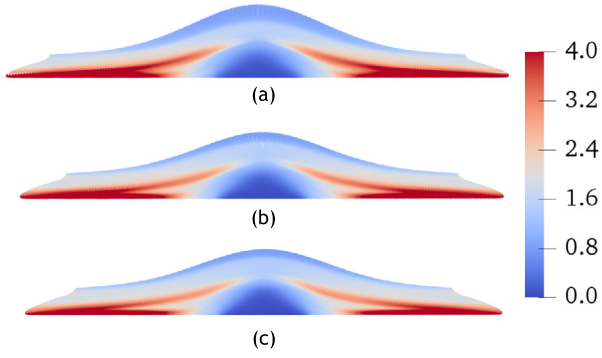

Fig. 29. Contours of ε_s on the final deposit configuration from simulations with (a) s_1 = 0 kPa, (b) s_2 = 25 kPa, and (c) s_3 = 50 kPa for $a_2 = 0.5$.

4.2.3. Influence of substrate roughness

We investigate the influence of substrate roughness on the soil column collapse by running simulations with different friction coefficients of the substrate, i.e., $\mu_{f1} = 0$, $\mu_{f2} = 0.25$, and $\mu_{f3} = 0.5$. The simulations are repeated for the specimens with the above three initial aspect ratios. Figs. 33–35 present the contours of ε_d in the final deposit configuration for the simulations with different initial aspect ratios. The results show that the roughness of the substrate could strongly influence the final deposit morphology. This effect increases for the cases with smaller initial aspect ratios. For $a_1 = 2$, the final deposit morphology is in a triangular shape when the substrate is perfectly

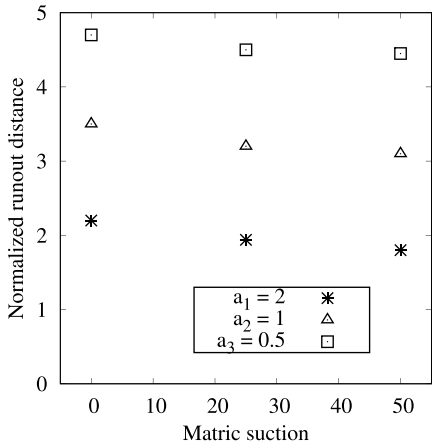

Fig. 30. Normalized final runout distance for simulations with different initial matric suctions.

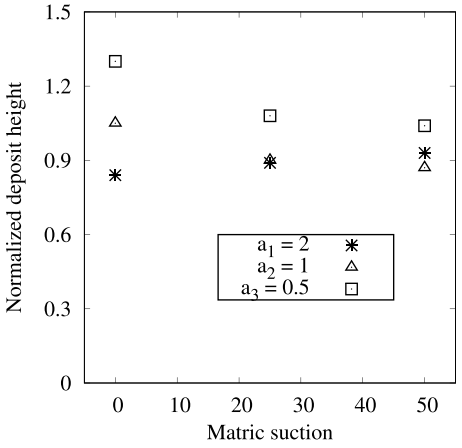

Fig. 31. Normalized final deposit height for simulations with different initial matric suctions.

smooth. Increasing the surface roughness of the substrate causes the final deposit morphology to transition to a more parabolic shape. For the case of $a_2 = 1$ as shown in Fig. 34 the final deposit morphology for a smooth substrate has concave slopes. Increasing the substrate roughness changes the final morphology to a more convex shape. For the case of $a_3 = 0.5$ increasing the substrate friction reduces the runout distance of the bottom layer along the substrate while the upper layer of soil has a larger runout distance as μ_f increases. Figs. 36 and 37 present the normalized final runout distance and the deposit height. The results show that the increasing substrate friction could decrease the final runout distance for the specimens with all aspect ratios. For the specimens with larger aspect ratios the deposit height generally increases with larger substrate frictions. However, for the specimen with $a_1 = 2$, the substrate friction has mild influence on the final deposit height as shown in Fig. 37.

Finally, Fig. 38 compares ε_s at the selected points from the simulations using different substrate frictions μ_f (see Fig. 16). The results in Fig. 38 show that ε_s at the points is independent of the substrate friction in the early stages of the collapse for all aspect ratios while the substrate friction does affect the maximum shear strain. It could be concluded that the substrate friction influences the final run-out distance and flow behavior but not the collapse triggering mechanism. We note that there might be the cracking phenomenon in the soil column under certain circumstances, i.e., soil moisture and boundary conditions. In this case, the energy based crack criterion in the total Lagrangian peridynamics [16] can be used to model cracking in the proposed updated Lagrangian peridynamics.

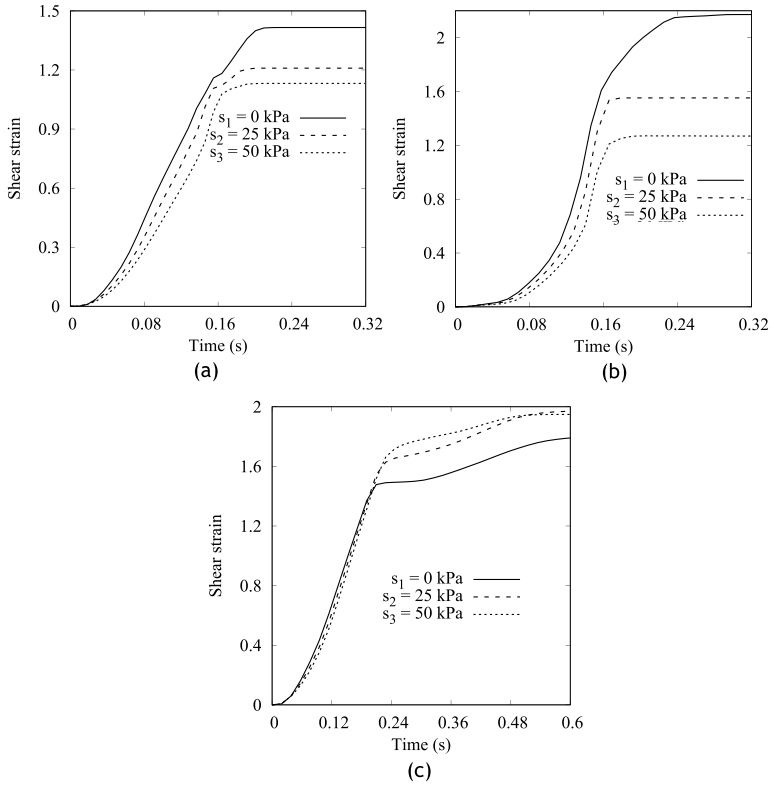

Fig. 32. Comparison of ε_s at the selected locations from simulations using different initial matric suctions with (a) $a_1 = 2$, (b) $a_2 = 1$ and (c) $a_3 = 0.5$.

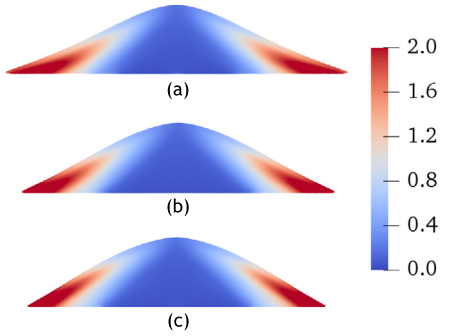

Fig. 33. Contours of ε_s from the simulations using (a) $\mu_{f1} = 0$, (b) $\mu_{f2} = 0.25$, and (c) $\mu_{f3} = 0.5$ for $a_1 = 2$.

5. Closure

In this article, we have formulated an updated Lagrangian peridynamics paradigm for modeling extreme large deformation in unsaturated porous media under drained conditions (i.e., constant matric suction). In this updated Lagrangian framework it is assumed that the family of a material point is a uniform sphere (i.e., constant horizon) independent of deformation. In this study, the bond-associated sub-horizon concept is utilized to eliminate the zero-energy modes at extreme large deformation of solid skeleton when using the correspondence constitutive models of unsaturated porous media. The stabilized nonlocal velocity gradient in the deformed configuration is used to numerically implement a critical state based visco-plastic model for unsaturated soils. The updated Lagrangian peridynamics framework is numerically implemented through the explicit Newmark scheme for high-performance computing. The uniaxial compression testing of a rectangular porous material specimen is first

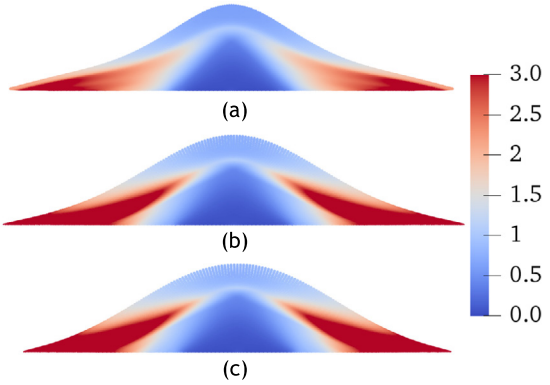

Fig. 34. Contours of ε_s from the simulations using (a) $\mu_{f1} = 0$, (b) $\mu_{f2} = 0.25$, and (c) $\mu_{f3} = 0.5$ for $a_2 = 1$.

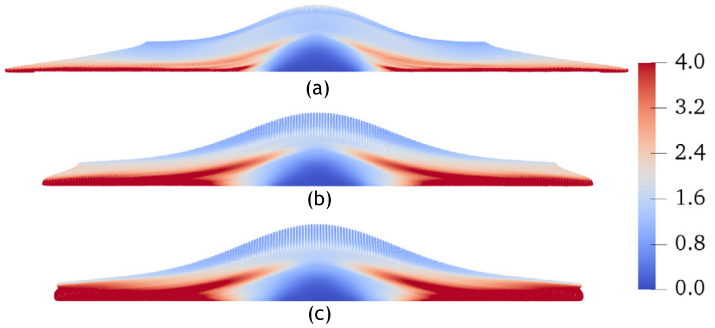

Fig. 35. Contours of ε_s from the simulations using (a) $\mu_{f1} = 0$, (b) $\mu_{f2} = 0.25$, and (c) $\mu_{f3} = 0.5$ for $a_3 = 0.5$.

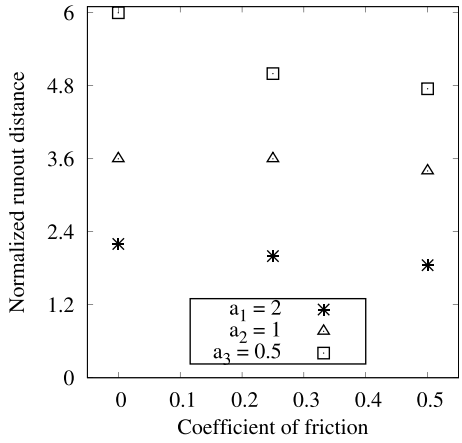

Fig. 36. Normalized final runout distance for different substrate frictions.

presented to demonstrate the stability of the updated Lagrangian periporomechanics paradigm under static and dynamic loads. We then conduct the numerical modeling of soil column collapse to demonstrate the efficacy and robustness of the updated Lagrangian periporomechanics paradigm in modeling extreme large deformation in unsaturated porous media under drained conditions. The numerical results have been validated against the experimental data in the literature. We also investigate the influence of initial matric suction and substrate friction on the final deposit morphology. The preliminary numerical results have shown that the impact of initial matric suction on the final run-out distance and deposit height may also depend on initial aspect ratios.

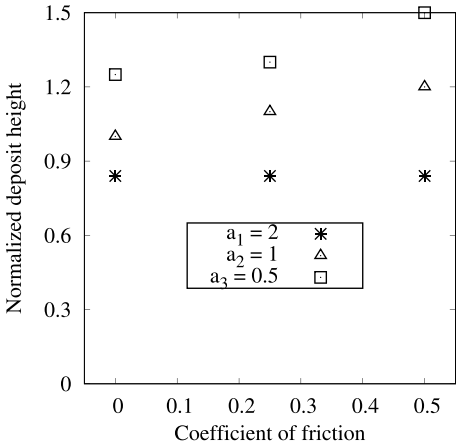

Fig. 37. Normalized final deposit height for different substrate frictions.

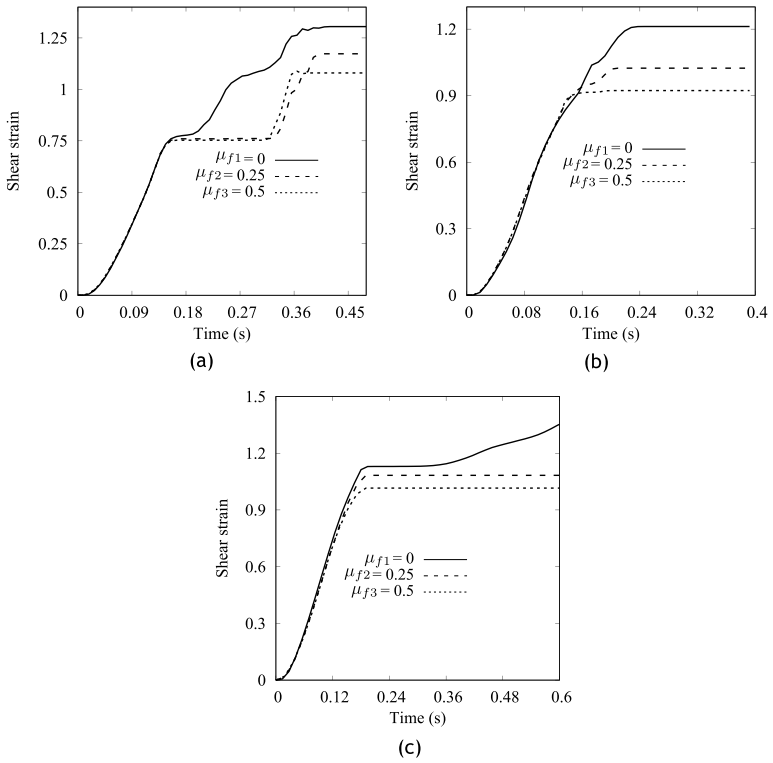

Fig. 38. Comparison of ε_s at the marked point for (a) $a_1 = 2$, (b) $a_2 = 1$ and (c) $a_3 = 0.5$ from simulations using different substrate frictions.

Declaration of competing interest

The authors declare the following financial interests/personal relationships which may be considered as potential competing interests: Xiaoyu Song reports financial support was provided by National Science Foundation.

Data availability

Data will be made available on request.

Acknowledgments

This work has been supported by the US National Science Foundation under contract numbers 1659932 and 1944009. The support is greatly acknowledged. We thank Professor Manolis Papadrakakis for his comments on the original version of this article. We also thank the three anonymous reviewers for their expert reviews of this article.

References

[1] X. Song, Menon S., Modeling of chemo-hydromechanical behavior of unsaturated porous media: a nonlocal approach based on integral equations, Acta Geotech. 14 (3) (2019) 727–747.
[2] X. Song, N. Khalili, A peridynamics model for strain localization analysis of geomaterials, Int. J. Numer. Anal. Methods Geomech. 43 (1) (2019) 77–96.
[3] X. Song, S.A. Silling, On the peridynamic effective force state and multiphase constitutive correspondence principle, J. Mech. Phys. Solids 145 (2020) 104161.
[4] S. Menon, X. Song, A computational periporomechanics model for localized failure in unsaturated porous media, Comput. Methods Appl. Mech. Engrg. 384 (2021) 113932.
[5] S. Menon, X. Song, A stabilized computational nonlocal poromechanics model for dynamic analysis of saturated porous media, Internat. J. Numer. Methods Engrg. (2021).
[6] K. Terzaghi, R.B. Peck, Soil Mechanics, Engineering Practice John Wiley and Sons, Inc, New York, 1948.
[7] R.W. Lewis, B. Schrefler, The Finite Element Method in the Static and Dynamic Deformation and Consolidation of Porous Media, John Wiley & Sons, 1998.
[8] O.C. Zienkiewicz, M. Chan A. Pastor, B. Schrefler, T. Shiomi, Computational Geomechanics, vol. 613, Citeseer, 1999.
[9] O. Coussy, Poromechanics, John Wiley & Sons, 2004.
[10] A.H.D. Cheng, Poroelasticity, vol. 27, Springer, 2016.
[11] D.G. Fredlund, H. Rahardjo, M.D. Fredlund, Unsaturated Soil Mechanics in Engineering Practice, John Wiley & Sons, 2012.
[12] X. Song, M. Ye, K. Wang, Strain localization in a solid-water-air system with random heterogeneity via stabilized mixed finite elements, International Journal for Numerical Methods in Engineering 112 (13) (2017) 1926–1950.
[13] S. Silling, Reformulation of elasticity theory for discontinuities and long-range forces, J. Mech. Phys. Solids 48 (1) (2000) 175–209.
[14] S.A. Silling, M. Epton, O. Weckner, J. Xu, E. Askari, Peridynamic states and constitutive modeling, J. Elasticity 88 (2) (2007) 151–184.
[15] S. Menon, X. Song, Shear banding in unsaturated geomaterials through a strong nonlocal hydromechanical model, Eur. J. Environ. Civ. Eng. (2020) 1–15.
[16] S. Menon, X. Song, Computational multiphase periporomechanics for unguided cracking in unsaturated porous media, Internat. J. Numer. Methods Engrg. 123 (12) (2022) 2837–2871.
[17] S.A. Silling, R.B. Lehoucq, Peridynamic theory of solid mechanics, Adv. Appl. Mech. 44 (2010) 73–168.
[18] E. Madenci, E. Oterkus, Peridynamic Theory and its Applications, Springer, 2014.
[19] X. Song, R.I. Borja, Mathematical framework for unsaturated flow in the finite deformation range, Internat. J. Numer. Methods Engrg. 97 (9) (2014) 658–682.
[20] X. Song, R.I. Borja, Finite deformation and fluid flow in unsaturated soils with random heterogeneity, Vadose Zone J. 13 (5) (2014).
[21] T. Belytschko, W.K. Liu, B. Moran, K. Elkhodary, Nonlinear Finite Elements for Continua and Structures, John Wiley & Sons, 2014.
[22] G.L. Bergel, S. Li, The total and updated lagrangian formulations of state-based peridynamics, Comput. Mech. 58 (2) (2016) 351–370.
[23] F. Bobaru, J.T. Foster, P.H. Geubelle, S.A. Silling, Handbook of Peridynamic Modeling, CRC Press, 2016.
[24] S.A. Silling, M.L. Parks, J.R. Kamm, O. Weckner, M. Rassaian, Modeling shockwaves and impact phenomena with eulerian peridynamics, Int. J. Impact Eng. 107 (2017) 47–57.
[25] S.A. Silling, Stability of peridynamic correspondence material models and their particle discretizations, Comput. Methods Appl. Mech. Engrg. 322 (2017) 42–57.
[26] S.A. Silling, E. Askari, A meshfree method based on the peridynamic model of solid mechanics, Comput. Struct. 83 (17–18) (2005) 1526–1535.
[27] M. Breitenfeld, P.H. Geubelle, O. Weckner, S. Silling, Non-ordinary state-based peridynamic analysis of stationary crack problems, Comput. Methods Appl. Mech. Engrg. 272 (2014) 233–250.
[28] M.R. Tupek, R. Radovitzky, An extended constitutive correspondence formulation of peridynamics based on nonlinear bond-strain measures, J. Mech. Phys. Solids 65 (1) (2014) 82–92.
[29] C.T. Wu, B. Ren, A stabilized non-ordinary state-based peridynamics for the nonlocal ductile material failure analysis in metal machining process, Comput. Methods Appl. Mech. Engrg. 291 (2015) 197–215.
[30] P. Li, Z.M. Hao, W.Q. Zhen, A stabilized non-ordinary state-based peridynamic model, Comput. Methods Appl. Mech. Engrg. 339 (2018) 262–280.
[31] X. Gu, Q. Zhang, E. Madenci, X. Xia, Possible causes of numerical oscillations in non-ordinary state-based peridynamics and a bond-associated higher-order stabilized model, Comput. Methods Appl. Mech. Engrg. 357 (2019) 112592.
[32] H. Chen, Bond-associated deformation gradients for peridynamic correspondence model, Mech. Res. Commun. 90 (2018) 34–41.
[33] S. Roy Chowdhury, P. Roy, D. Roy, J.N. Reddy, A modified peridynamics correspondence principle: Removal of zero-energy deformation and other implications, Comput. Methods Appl. Mech. Engrg. 346 (2019) 530–549.
[34] N.A. Hashim, W. Coombs, C. Augarde, G. Hattori, An implicit non-ordinary state-based peridynamics with stabilised correspondence material model for finite deformation analysis, Comput. Methods Appl. Mech. Engrg. 371 (2020) 113304.

[35] S.R. Chowdhury, P. Roy, D. Roy, J. Reddy, A modified peridynamics correspondence principle: Removal of zero-energy deformation and other implications, Comput. Methods Appl. Mech. Engrg. 346 (2019) 530–549.
[36] E. Gabriel, G.E. Fagg, G. Bosilca, T. Angskun, J.J. Dongarra, J.M. Squyres, V. Sahay, P. Kambadur, B. Barrett, A. Lumsdaine, et al., Open Mpi: Goals, Concept, and Design of a Next Generation Mpi Implementation, Springer, 2004, pp. 97–104.
[37] S. Utili, T. Zhao, G. Houlsby, 3D dem investigation of granular column collapse: evaluation of debris motion and its destructive power, Eng. Geol. 186 (2015) 3–16.
[38] E. Lajeunesse, C. Quantin, P. Allem, C. Delacourt, New insights on the runout of large landslides in the valles-marineris canyons, mars, Geophys. Res. Lett. 33 (4) (2006).
[39] N. Lu, J.W. Godt, Hillslope Hydrology and Stability, Cambridge University Press, 2013.
[40] E.E. Alonso, Triggering and motion of landslides, Géotechnique 71 (1) (2021) 3–59.
[41] M. Krantz, H. Zhang, J. Zhu, Characterization of powder flow: Static and dynamic testing, Powder Technol. 194 (3) (2009) 239–245.
[42] M. Trolese, M. Cerminara, T.E. Ongaro, G. Giordano, The footprint of column collapse regimes on pyroclastic flow temperatures and plume heights, Nature Commun. 10 (1) (2019) 1–10.
[43] E. Lajeunesse, A. Mangeney-Castelnau, J.P. Vilotte, Spreading of a granular mass on a horizontal plane, Phys. Fluids 16 (7) (2004) 2371–2381.
[44] G. Lube, H.E. Huppert, R.S.J. Sparks, M.A. Hallworth, Axisymmetric collapses of granular columns, J. Fluid Mech. 508 (2004) 175–199.
[45] G. Crosta, S. Imposimato, D. Roddeman, Numerical modeling of 2-d granular step collapse on erodible and nonerodible surface, J. Geophys. Res.: Earth Surface 114 (F3) (2009).
[46] H.H. Bui, R. Fukagawa, K. Sako, S. Ohno, Lagrangian meshfree particles method (sph) for large deformation and failure flows of geomaterial using elastic–plastic soil constitutive model, Int. J. Numer. Anal. Methods Geomech. 32 (12) (2008) 1537–1570.
[47] S. Dunatunga, K. Kamrin, Continuum modelling and simulation of granular flows through their many phases, J. Fluid Mech. 779 (2015) 483–513.
[48] C.M. Mast, P. Arduino, P. Mackenzie-Helnwein, G.R. Miller, Simulating granular column collapse using the Material Point Method, Acta Geotech. 10 (1) (2015) 101–116.
[49] D. Salciarini, C. Tamagnini, P. Conversini, Discrete element modeling of debris-avalanche impact on earthfill barriers, Phys. Chem. Earth, Parts A/B/C 35 (3–5) (2010) 172–181.
[50] W. Sun, J.T. Ostien, A.G. Salinger, A stabilized assumed deformation gradient finite element formulation for strongly coupled poromechanical simulations at finite strain, Int. J. Numer. Anal. Methods Geomech. 37 (16) (2013) 2755–2788.
[51] R.I. Borja, Plasticity, vol. 2, Springer, 2013.
[52] K. Oliynyk, M.O. Ciantia, C. Tamagnini, A finite deformation multiplicative plasticity model with non–local hardening for bonded geomaterials, Comput. Geotech. 137 (2021) 104209.
[53] T. Ni, F. Pesavento, M. Zaccariotto, U. Galvanetto, Q.Z. Zhu, B.A. Schrefler, Hybrid fem and peridynamic simulation of hydraulic fracture propagation in saturated porous media, Comput. Methods Appl. Mech. Engrg. 366 (2020) 113101.
[54] T. Ni, F. Pesavento, M. Zaccariotto, U. Galvanetto, B.A. Schrefler, Numerical simulation of forerunning fracture in saturated porous solids with hybrid fem/peridynamic model, Comput. Geotech. 133 (2021) 104024.
[55] E.E. Alonso, A. Gens, A. Josa, A constitutive model for partially saturated soils, Géotechnique 40 (3) (1990) 405–430.
[56] C. Chiu, C.W.W. Ng, A state-dependent elasto-plastic model for saturated and unsaturated soils, Géotechnique 53 (9) (2003) 809–829.
[57] X. Song, K. Wang, B. Bate, A hierarchical thermo-hydro-plastic constitutive model for unsaturated soils and its numerical implementation, Int. J. Numer. Anal. Methods Geomech. 42 (15) (2018) 1785–1805.
[58] A.H. Cheng, A linear constitutive model for unsaturated poroelasticity by micromechanical analysis, Int. J. Numer. Anal. Methods Geomech. 44 (4) (2020) 455–483.
[59] M.T. Van Genuchten, A closed-form equation for predicting the hydraulic conductivity of unsaturated soils, Soil Sci. Am. J. 44 (5) (1980) 892–898.
[60] N. Lu, W. Likos, Unsaturated Soil Mechanics, John Wiley & Sons, 2004.
[61] C.W.W. Ng, B. Menzies, Advanced Unsaturated Soil Mechanics and Engineering, CRC Press, 2014.
[62] J. Cao, J. Jung, X. Song, B. Bate, On the soil water characteristic curves of poorly graded granular materials in aqueous polymer solutions, Acta Geotech. 13 (1) (2018) 103–116.
[63] W.J. Niu, W.M. Ye, X. Song, Unsaturated permeability of gaomiaozi bentonite under partially free-swelling conditions, Acta Geotech. 15 (5) (2020) 1095–1124.
[64] X. Song, Transient bifurcation condition of partially saturated porous media at finite strain, Int. J. Numer. Anal. Methods Geomech. 41 (1) (2017) 135–156.
[65] J.C. Simo, T.J. Hughes, Computational Inelasticity, vol. 7, Springer Science & Business Media, 1998.
[66] R. Conti, C. Tamagnini, A. DeSimone, Critical softening in cam-clay plasticity: Adaptive viscous regularization, dilated time and numerical integration across stress–strain jump discontinuities, Comput. Methods Appl. Mech. Engrg. 258 (2013) 118–133.
[67] R.I. Borja, Cam-clay plasticity. part v: A mathematical framework for three-phase deformation and strain localization analyses of partially saturated porous media, Comput. Methods Appl. Mech. Engrg. 193 (48–51) (2004) 5301–5338.
[68] R.I. Borja, X. Song, W. Wu, Critical state plasticity. part vii: triggering a shear band in variably saturated porous media, Computer Methods in Applied Mechanics and Engineering 261 (2013) 66–82.
[69] T.J. Hughes, The finite element method: linear static and dynamic finite element analysis, Courier Corp. (2012).
[70] D.J. Littlewood, T. Shelton, J.D. Thomas, Estimation of the Critical Time Step for Peridynamic Models, Tech. Rep., Sandia National Lab.(SNL-NM), Albuquerque, NM (United States, 2013.

[71] S.A. Silling, Meshfree Peridynamics for Soft Materials, Tech. Rep., Sandia National Lab.(SNL-NM), Albuquerque, NM (United States, 2016.
[72] K. Wang, X. Song, Strain localization in non-isothermal unsaturated porous media considering material heterogeneity with stabilized mixed finite elements, Comput. Methods Appl. Mech. Engrg. 359 (2020) 112770.